10

Decompression
10.1 Decompression Theory

Peter Tikuisis and Wayne A Gerth

The tissues of an air-breathing organism are obliged under the Second Law of Thermodynamics to seek equilibrium with the gas respired by the organism. The conditions for this equilibrium vary with the pressure and composition of the respired gas, but are only approached over time after the motivating change in respired gas occurs. Any change in the respired gas pressure or composition is consequently followed by a period in which the tissues are in thermodynamic dysequilibrium. Atmospheric decompression produces dysequilibria in which tissues contain excessive amounts of dissolved atmospheric gas. If the decompression is sufficiently rapid and extensive, the dissolved gas excess in certain tissues causes a phase dysequilibrium that can either be sustained metastably, while the excess gas is eliminated harmlessly by physiologic means, or relieved in situ by the evolution of gas bubbles. Such bubble formation can in turn cause one or more of a variety of pathologic symptoms and signs in humans that are collectively known as decompression sickness (DCS).

The task of decompression theory is to elucidate the factors and processes that govern the occurrence of DCS for use in the control of atmospheric decompressions to limit the incidence and severity of DCS. This is an intrinsically quantitative task that requires conceptualization, then mathematical representation, of the processes involved as they behave under the influences of recognized governing factors. Substantial simplifications are inevitably required due to ignorance or to achieve mathematical tractability. In the following, we provide an overview of the basic concepts and mathematical representations on which modern theories of decompression are based, endeavoring to adopt formalism sufficient only to illuminate some of the simplifications that are made. We then review how these concepts have been integrated into quantitative models for control of decompression to limit the incidence and severity of DCS. The application of these models to the development of decompression procedures is discussed in Chapter 10.2. The overwhelming pathophysiologic link between bubbles and DCS has been amply reviewed by Vann & Thalmann, (1993) and by Francis & Mitchell in Chapter 10.4 and will not be covered here.

BASIC CONCEPTS

The paradigm for the pathophysiology of DCS that has emerged from decompression research to date, and that motivates the organization of this overview, is schematized in Fig. 10.1.1. The central feature of this paradigm is that various processes cause transitions of tissues into different thermodynamic states indicated in the rectangles. For example, decompression can cause transition of one or more tissues from a gas-saturated state into a gas-supersaturated state. The latter is relieved with return to a gas-saturated state either by physiologic gas elimination or by in situ nucleation and growth of gas bubbles. The latter process may in turn cause DCS. The remainder of this section is devoted to discussion of these different states and the processes by which transitions occur between them.

THE GAS-SATURATION STATE

Control of tissue gas-saturation states is central to the prevention of DCS. For any given tissue, these states are defined in thermodynamic terms as for any liquid; i.e. by reference to the pressure–volume properties of a gas phase that would be in equilibrium with the liquid, as schematized in Fig. 10.1.2. Each of the three isothermal systems shown consists of a gas phase in equilibrium with a liquid phase across a planar gas–liquid

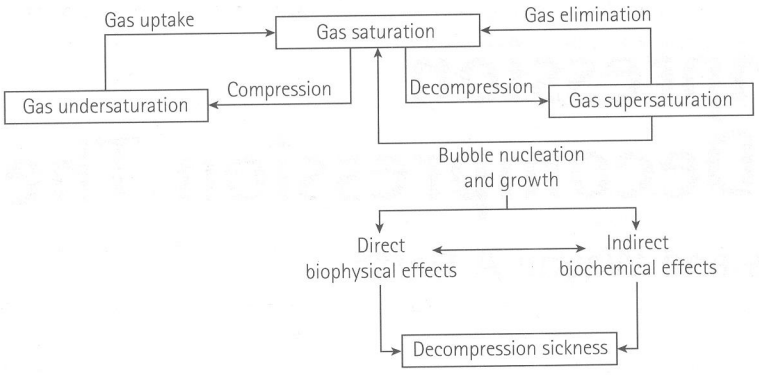

Fig. 10.1.1 Schematic of the current paradigm for the occurrence of DCS.

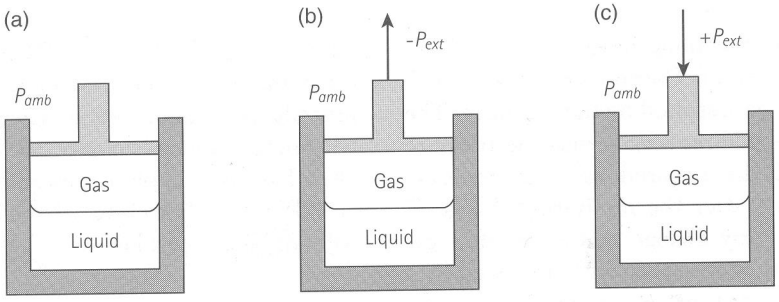

Fig. 10.1.2 Three different isothermal systems consisting of a gas phase in equilibrium with a liquid phase across a planar gas–liquid interface at which hydrostatic pressures in gas and liquid are equal. The gas and liquid phases in each system are separated from the atmosphere at pressure P_{amb} by a weightless and frictionless piston. P_{amb} can be considered to represent the pressure at surface (i.e. 101 kPa, 1.0 ATA). The piston in system (a) is at equilibrium in the position shown with no applied external pressure. The pistons in systems (b) and (c) are maintained in the positions shown by applied external pressures in directions indicated by the arrows. The net pressure exerted on the system is the sum of P_{amb} and P_{ext}.

interface at which hydrostatic pressures in gas and liquid are equal. As schematics of tissue gas-saturation states, the liquid and gas phases in these systems have properties that are interchangeable with properties of tissues and gases, respectively, in vivo. For simplicity, gravitational forces in the systems are neglected. If the gas phase in each system is considered to be ideal and composed of any number of gas components (denoted by the subscript i), Dalton's law of partial pressures states that the sum of gas partial pressures in the gas phase (ΣP_i) equals the hydrostatic pressure in the gas phase. Because the systems are at equilibrium, each gas partial pressure equals its corresponding gas tension in the liquid phase; $p_i = P_i$; so that $\Sigma p_i = \Sigma P_i$. Note the terminology of pressure (P) and tension (p) refer to the presence of gas in the gas and liquid phases, respectively, yet both share the same units (e.g. kPa, ATA, msw, etc.). Liquid vapor is an ever-present component of the gas phase in each of these systems. Thus water vapor, with a partial pressure dependent on temperature only, constitutes a small but constant component [6.2 kPa (0.062 ATA) at 37°C] in human physiologic tissue.

If the gas phase in each of the illustrated systems contains one or more gases in addition to liquid vapor, the external pressures exerted by the pistons are direct measures of the liquid phase gas-saturation states with respect to P_{amb}. In system (a), the external pressure is zero, and thus the sum of the gas partial pressures in the gas phase including the vapor pressure, ΣP_i, equals P_{amb}, and the liquid is gas saturated with respect to P_{amb}. In each of the other systems, the magnitude and direction of the external pressure determines the magnitude of liquid phase gas undersaturation (negative P_{ext}) or gas supersaturation (positive P_{ext}) with respect to P_{amb}.

In system (b), negative external pressure acts to keep the system pressure less than P_{amb} by an amount equal to P_{ext}. The liquid in such a system is gas undersaturated with respect to P_{amb} by this amount. Release of the external pressure allows the system pressure to relax to P_{amb}. This occurs via a diminution of the gas phase volume from a Boyle's law effect, and from liquid

vapor condensation and gas dissolution into the liquid. If the gas phase is completely consumed by the liquid after the force on the piston is removed, then the liquid will remain somewhat gas undersaturated ($\Sigma p_i < P_{amb}$) but completely stable at hydrostatic pressure P_o.

In system (c), positive external pressure acts to keep the system pressure greater than P_{amb} by an amount equal to P_{ext}. The liquid in such a system is gas supersaturated with respect to P_{amb} by an amount $P_{ss} = P_{ext}$, hence:

$$P_{ss} = \Sigma p_{liquid} - P_{amb}. \quad (1)$$

Release of the external pressure (decompression) results in an expansion of the gas phase volume. If the system begins with no initial gas phase, then it is considered unstable and the only way it can attain equilibrium is through the formation and expansion of a gas phase. Moreover, because the gas-supersaturated condition is an intrinsic property of the liquid (Lewis & Randall 1961), this gas phase formation and growth can occur at any point within the liquid. A gas-supersaturated liquid is thus in phase dysequilibrium with respect to P_{amb}; a condition in tissue that can have grave consequences. We will consider the stability of a liquid in this state when we examine the mechanisms of bubble nucleation.

Implicit from the above is that gas supersaturation is defined in terms of the total dissolved gas tension, not in terms of any particular gas component in the system. Thus, a liquid can be oversaturated with a given component gas in a multigas system without being gas supersaturated. Such a condition is one of chemical dysequilibrium but not phase dysequilibrium. Another measure of gas supersaturation without any direct thermodynamic interpretation is the gas supersaturation ratio, or 'tissue ratio' (TR), defined by:

$$TR = \Sigma p_{tissue}/P_{amb}. \quad (2)$$

GAS CONCENTRATION

In each of the systems of Fig. 10.1.2 at equilibrium, the composition of either phase is determined completely by the composition of the other phase. Gas components that do not interact with saturable sites on macromolecules or combine chemically with any other components of the liquid (or tissue), dissolve in the liquid according to Henry's law, which states that the concentration (c) of a gas in the liquid phase is proportional to its gas tension. Such gas components are considered inert in diving physiology. The proportionality constant is the Ostwald solubility coefficient [α in ml gas/ml/atm at ambient temperature (Weathersby & Homer, 1980)]; e.g. in blood:

$$c_{blood} = \frac{\alpha_{blood} \cdot p_{blood}}{kT}, \quad (3)$$

where k is the Boltzmann gas constant and T is the absolute temperature. Accepted values of α_{blood} at 37°C for N_2 (nitrogen) and He (helium), the principal inert gases used in diving, are 0.0158 and 0.0104, respectively (Christoforides & Hedley-Whyte 1970). Consequently, at saturation under the same ambient partial pressures (or dissolved gas tensions), 52% more N_2 is dissolved in blood than is He.

The oxygen content of blood consists of O_2 dissolved in the blood plasma, which follows Henry's law, but also of O_2 bound to saturable sites on hemoglobin. The equilibrium O_2 concentration in blood as a function of the blood O_2 tension, pO_2, is closely approximated by (Lobdell 1981):

$$c_{blood,O_2} = p_{O_2}\,\alpha_{plasma,O_2} + Hbg \cdot \left\{ \frac{a \cdot \left(\frac{p_{O_2}}{p_{50}}\right)^n + b \cdot \left(\frac{p_{O_2}}{p_{50}}\right)^{2n}}{1 + c \cdot \left(\frac{p_{O_2}}{p_{50}}\right)^n + b \cdot \left(\frac{p_{O_2}}{p_{50}}\right)^{2n}} \right\}, \quad (4)$$

where Hbg is the O_2 carrying capacity of 100% O_2-saturated hemoglobin in the blood (cc O_2 per100 cc blood) and the factor within the large brackets gives the fraction of Hb saturation. The constants in the latter factor, determined by fit to measured human Hb-O_2 saturation curves, are: $a = 0.34332$, $b = 0.64073$, $c = 0.34128$, $n = 1.58678$, and p_{50} is the pO_2 at which the hemoglobin is half-saturated. The plot of Equation 4 in Fig. 10.1.3 illustrates that O_2 solubility in blood is a highly non-linear function of O_2 partial pressure in the normal physiologic range of O_2 pressures.

GAS EXCHANGE

The gas saturation states described above are reached in tissue via the circulation of blood as the tissue seeks equilibrium with the atmosphere by absorbing or desorbing gas to equalize partial pressures between tissue and atmosphere. This equilibration is attained in two steps; first between atmosphere and blood in the lungs, and second between blood and tissue in the various regions of the body. The kinetics of these gas exchanges govern the gas saturations attained in various tissues during compression, and the magnitudes and time courses of gas supersaturations attained during and after decompression.

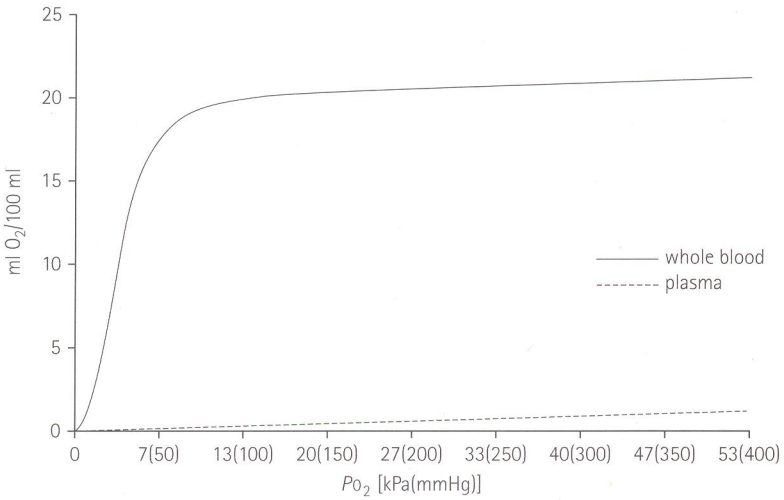

Fig. 10.1.3 Oxygen solubility in whole blood as a function O_2 partial pressure [*Hbg* = 20 ccO_2 per 100 cc blood; p_{50} = 3.3 kPa (25 mmHg)]. At O_2 partial pressures in excess of about 20 kPa (150 mmHg), the hemoglobin is fully oxygenated and any further absorption of O_2 follows the Henry's law slope (dotted line) for O_2 solubility in plasma.

Since the inert gases, N_2 and He, are sparingly soluble in blood and the exposure time between the inspired gas and pulmonary blood is sufficiently long for equilibration (Hills 1977), gas partial pressures in arterial blood are usually assumed equivalent to alveolar gas partial pressures. It should be noted, however, that small alveolar–arterial partial pressure differences due to ventilation–perfusion mismatch occur in the normal lung, and that these may be further exacerbated by bubbles in the pulmonary arterial blood, breathing of oxygen at high partial pressures, and high transpulmonary fluxes of inert gas (Brubakk et al 1999, Farhi & Olszowka 1968, Olszowka & Farhi 1969). Notwithstanding these asymmetries in blood–lung gas exchange, primary strategies to understand and prevent DCS are focussed on the kinetics of blood–tissue gas exchange.

All strategies begin with the assumption pioneered by Boycott et al (1908) that the whole body is a collection of m parallel-perfused compartments, as schematized in Fig. 10.1.4. The different strategies then diverge from one another in the number of compartments considered and in how the gas exchanges in any given compartment are characterized. The compartments need not be explicitly associated with specific anatomical tissues, because blood flow and other properties relevant to gas exchange are not uniform throughout any one tissue (Homer & Weathersby 1986, Homer et al 1990). Thus, the terms 'compartment' and 'tissue' are used synonymously to denote a non-descript site or sites that share the same gas exchange properties but that may actually represent a collection of different anatomic sites throughout the body. It is interesting in this regard

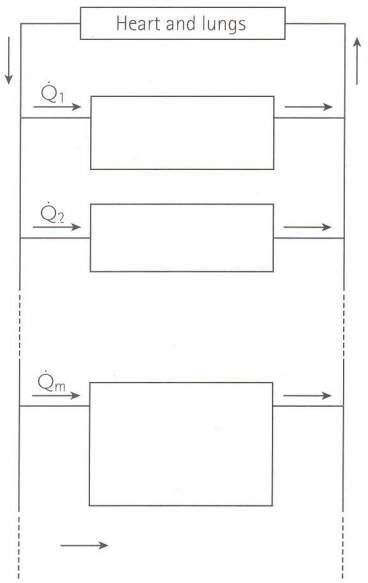

Fig. 10.1.4 Schematic of m parallel-perfused compartment model of the whole body. The arrows indicate arterial and venous blood flow, and $\dot{Q}$ is the blood perfusion rate. Association of compartments with specific anatomical sites is usually disclaimed except to assert that the modeled compartments represent tissues or tissue components that are involved in the occurrence of DCS.

that Weathersby et al (1981) concluded from tissue gas distribution studies that a single kinetic parameter per tissue is generally adequate to model blood–tissue gas exchange. More recently, Flook (1998) adopted the Mapleson (1963) multitissue model to numerically

balance total gas uptake and elimination in a physiologic model of decompression.

In general, the rate at which the concentration of a gas changes at any point in a tissue is given by the combined Fick-Fourier diffusion-rate equation (Wienke 1989):

$$\frac{dc}{dt} = \nabla(D \cdot \nabla c) + \frac{\dot{Q}}{V_t} \cdot (c_{a,g} - c_{v,g}) - Z'_{met,g} - Z'_{b,g}, \quad (5)$$

where t is time, ∇ is the spatial gradient operator, D is the diffusion coefficient of the gas in the tissue, $\dot{Q}$ is the blood perfusion rate (ml blood/min), V_t is the tissue volume (ml), $c_{a,g}$ and $c_{v,g}$ are the respective gas concentrations in arterial and end-capillary or venous blood (ml gas/ml blood), and $Z'_{met,g}$ and $Z'_{b,g}$ are the respective rates of gas consumption by metabolism and bubble growth (ml gas/ml tissue/min). The first term on the right side of this expression is the contribution of diffusion, while the remaining terms give the contributions of perfusion, metabolism, and bubble dynamics, respectively. Because N_2 and He are neither the reactants nor products of any metabolic process in human tissue, the $Z'_{met,g}$ term in Equation 5 is zero for these gases. This is the sense in which these gases are considered 'inert' in diving physiology. If there are no bubbles in the tissue, the $Z'_{b,g}$ term also vanishes for all gases in the tissue.

PERFUSION-LIMITED GAS EXCHANGE

Most modern diving practices are based on theories in which Equation 5 is solved under the assumption that the tissue is well stirred; i.e. has a uniform dissolved gas concentration with no internal concentration gradients. Under this assumption, Equation 5 simplifies to:

$$\frac{dp_{t,g}}{dt} = \frac{\dot{Q}}{\alpha_{t,g} \cdot V_t}(p_{a,g} - p_{v,g}) - Z_{met,g} - Z_{b,g}, \quad (6)$$

where concentrations have been converted to partial pressures using Henry's law in Equation 3, and tissue gas solubilities, $\alpha_{t,g}$, have been incorporated into $Z_{met,g}$ and $Z_{b,g}$. Equation 6 simply states that the rate of change of gas tension in a tissue is equal to the rate of gas delivery by the blood minus the rate at which gas is consumed by metabolic processes and bubble growth. If gas exchange is perfusion limited, meaning that the venous gas tension is in complete equilibrium with the tissue gas tension, then $p_{t,g} = p_{v,g}$. Under this condition, the inert gas tension in a bubble-free tissue changes at a rate that is proportional to the difference between arterial and tissue gas tensions, as follows:

$$\frac{dp_{t,g}}{dt} = \frac{p_{a,g} - p_{t,g}}{\tau}, \quad (7)$$

where τ is the blood–tissue gas exchange time constant given by:

$$\tau = \frac{\alpha_{t,g}}{\dot{Q} \cdot \alpha_{blood,g}}. \quad (8)$$

The corresponding blood–tissue gas exchange half-time, $t_{1/2} = \tau \cdot ln\ 2$, gives the time required to halve an initial tissue–blood gas tension difference with constant τ and $p_{a,g}$. If the arterial gas tension changes in response to a time-linear change in inspired gas partial pressure, then $p_{a,g} = p^o_{a,g} + m_{a,g} \cdot t$, and Equation 7 becomes:

$$\frac{dp_{t,g}}{dt} = \frac{m_{a,g} \cdot t + (p^o_{a,g} - p_{t,g})}{\tau}, \quad (9)$$

where the superscript (o) refers to the initial value at $t = 0$ and $m_{a,g}$ is the rate of change of the arterial tension of the gas $(= dp_{a,g}/dt)$.

Tissues are considered 'fast' or 'slow' according to whether τ is small or large, respectively. Equation 8 indicates that τ increases with the tissue–blood gas partition coefficient, α_t/α_{blood}, of the gas. In general, for given blood perfusion rates, aqueous tissues with low gas solubilities are considered 'fast' (in terms of saturation time) whereas fatty tissues with high gas solubilities are 'slow.' In aqueous tissues, the tissue–blood gas partition coefficients are slightly above unity for the inert gases. Consequently, the saturation rates for different inert gases are approximately the same in such tissues, varying principally with only the blood perfusion rate. Tissue–blood gas partition coefficients in fatty tissues, on the other hand, vary more widely among the different inert gases. For example, α_{fat} values for N_2 and He are approximately 0.076 and 0.0168, respectively, according to their values in oil (Behnke & Yarbrough 1939). As a result, the time constant for N_2 in a fatty tissue is almost three times as large as that for He, so that the tissue saturates with N_2 considerably slower than with He at the same ambient partial pressures. It is important to note, however that at saturation under these conditions, the concentration of N_2 in fat is 452% higher than the concentration of He. These differences have important implications for the dynamics of bubble evolution in such tissues.

Equation 9 can be integrated to yield the tissue gas tension at time t:

$$p_{t,g} = p^o_{a,g} + m_{a,g} \cdot t + (p^o_{t,g} - p^o_{a,g}) \cdot e^{-(t/\tau)} - m_{a,g} \cdot \tau \cdot (1 - e^{-(t/\tau)}). \quad (10)$$

Solution of Equation 10 requires a continuous description of the pressure and respired gas profile. This is provided by encoding each profile as a sequence of nodes that

give the pressure or depth and the inspired gas composition at particular times in the profile (Weathersby et al 1992b). An unbroken description of the profile is then obtained by linear interpolation in the time domain between successive nodes. Each node thus gives the conditions prevailing at the end of a profile stage, that is:

1 a travel stage (compression or decompression);
2 an isobaric stage;
3 a breathing gas switch stage; or
4 a combination travel and breathing gas switch stage.

The model is then exercised on the profile by sequentially processing these stages, preserving the model state at the end of each stage as the initial state for the next stage.

Fig. 10.1.5 shows the N_2 and He tissue tensions prescribed by Equation 10 during a hypothetical in-water O_2 decompression dive to 43 msw (140 fsw) for 39 min on 84% He (balance O_2) followed by a staged decompression on air to 9 msw (30 fsw), 60 min on 100% O_2 with two 5 min air breaks at 9 msw (30 fsw), and surfacing on air [from DCIEM Diving Manual (DCIEM Diving Manual Part 2 1995)]. The inert gas uptake and elimination were computed using time constants of 60 and 27 min for N_2 and He, respectively, corresponding to tissue solubilities of 0.0459 and 0.0136 based on a hypothetical tissue composition of 50% blood and 50% fat. Not surprisingly, the tissue He tension quickly surpasses the tissue N_2 tension during the bottom time of the dive, but reverses during decompression. Note, however, that the concentration of N_2 is relatively high during the entire dive due to its much higher tissue solubility than He. As will be seen below, the amount of dissolved gas is pivotal to the development of bubbles. Hypothetically, if an inert gas of near zero solubility existed, then the availability of such a gas for bubble formation would be negligible. Unfortunately, no known breathable gas exists with a lower solubility than He in biological fluids/tissues (Weathersby & Homer 1980). Also relevant to bubble formation is the degree of gas supersaturation (P_{ss}). Note in this example that P_{ss} is positive, and that the tissue ratio, *TR*, exceeds unity only during the initial period of decompression (i.e. between 39 and 66 min). The magnitude and persistence of P_{ss} vary with the tissue time constants.

The kinetics of blood–tissue O_2 and CO_2 exchange are more complicated, not only because of the non-linearity of O_2 solubility in blood (Fig. 10.1.3), but also because these gases participate in tissue metabolism and require consideration of the $Z_{met,g}$ term in Equation 6 (Van Liew et al 1993, Yount & Lally 1980). Aerobic metabolism in tissue converts O_2 practically mole-for-

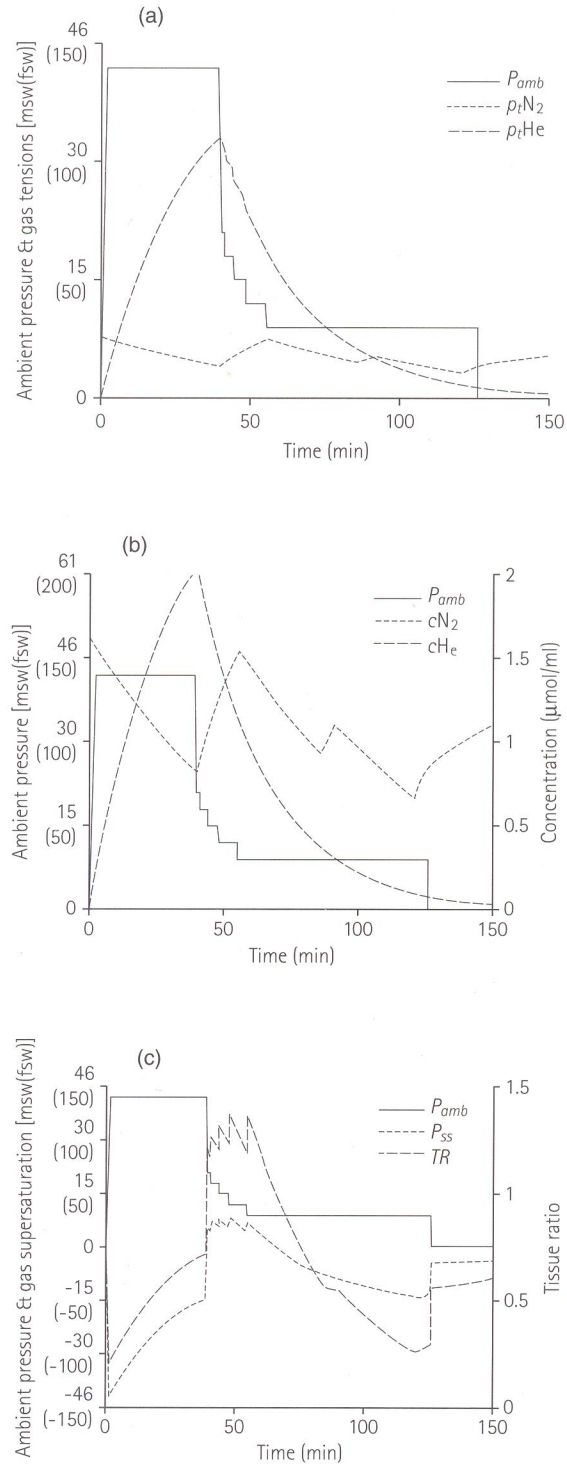

Fig.10.1.5 Profile for in-water decompression dive to 43 msw (140 fsw) 39 min where the ambient pressure (P_{amb}) is shown in msw gauge. Also shown are (a) tissue gas tension values (p_t) in msw absolute and based on time constants of 60 and 27 min for N_2 and He, respectively, (b) tissue gas concentrations (cf Equation 3), and (c) gas supersaturation (Equation 1) and the tissue ratio (Equation 2).

mole into carbon dioxide (CO_2), a much more soluble gas than the O_2 it replaces. The resultant total gas tension is correspondingly reduced. If the tissue O_2 consumption, Z_{met,O_2}, is independent of arterial p_{O_2}, its value is then given by that prevailing under steady-state conditions, i.e. when $dp_{t,O_2}/dt = 0$. Under this condition, and in the absence of bubbles so that the Z_{b,O_2} term vanishes, Equation 6 can be solved to yield Z_{met,O_2} as the product of the blood flow and the arterial–venous O_2 concentration difference, c_{av,O_2}:

$$Z_{met,O_2} = \dot{Q} \cdot (c_{a,O_2} - c_{v,O_2}) = \dot{Q} \cdot c_{av,O_2}, \qquad (11)$$

where Z_{met,O_2} is now in units of ml O_2/min. The right side of Equation 11 is then rearranged to obtain the following expression for the steady-state venous O_2 concentration:

$$c_{v,O_2} = c_{a,O_2} - c_{av,O_2}. \qquad (12)$$

The steady-state tissue O_2 tension that corresponds to the end-capillary O_2 concentration, c_{v,O_2}, given by Equation 12 varies with arterial p_{O_2}. Determination of this tension requires solution of Equation 4 for c_{a,O_2}, the arterial O_2 concentration at given p_{a,O_2}, then numerical inversion of Equation 4 for the partial pressure at the resultant $c_{a,O_2} - c_{av,O_2}$ difference. Steady-state tissue O_2 tensions as functions of arterial p_{O_2} for various tissue O_2 extractions are given in Fig. 10.1.6. Clearly, the resultant O_2 tensions are low at low p_{a,O_2} and high Z_{met,O_2}.

On this basis, and presuming that tissues involved in DCS have appreciable metabolic rates, inspired O_2 has been considered to manifest in tissue O_2 partial pressures that contribute minimally or not at all to DCS risk. In treatments that assume a small effect, a constant but low tissue O_2 tension is often assumed. CO_2 is also often assumed to be a constant contributor to the overall gas tension in all but pulmonary tissues. Together with water vapor, the constant p_{O_2} and p_{CO_2} then constitute a 'fixed' subset of Σp_i, which we will hereafter refer to as Σp_{fix}.

OXYGEN WINDOW

As a result of the metabolism of O_2, tissues are inherently undersaturated with gas prior to decompression, thus allowing some decompression without causing any tissue gas supersaturation. This opening, known as the 'oxygen window,' is illustrated in Fig. 10.1.7 as it varies with tissue metabolic rate and inspired O_2 fraction. The magnitude of the O_2 window is seen to decrease with decreasing ambient pressure at values of the latter below which hemoglobin in venous blood is fully O_2 saturated. The O_2 window thus depends in a complicated fashion on the inspired O_2 partial pressure and tissue metabolic rate.

The above effects of O_2 metabolism pertain to tissues at steady-state, which they are not after an atmospheric decompression. Oxygen can still contribute appreciably to the total dissolved gas tension before it reaches its steady-state tissue tension after completion of a decompression. As illustrated in Fig. 10.1.8, metabolism simply accelerates the approach to steady-state,

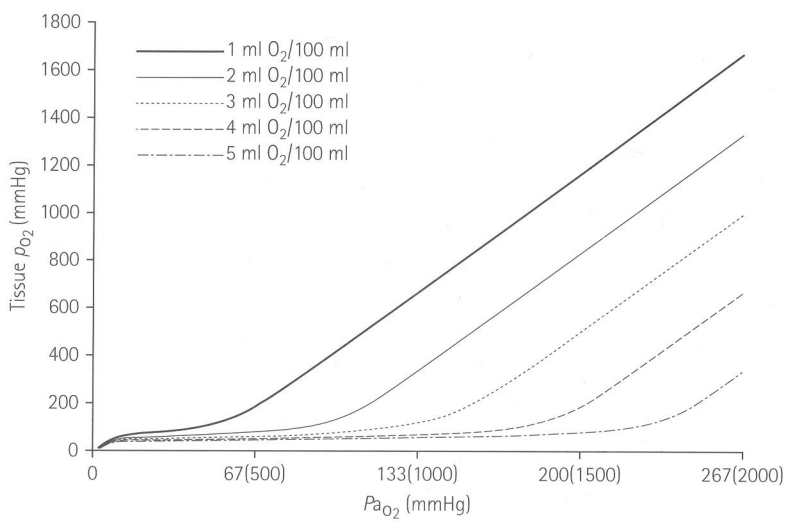

Fig. 10.1.6 Tissue O_2 tension under steady-state conditions as functions of arterial p_{O_2} for tissue O_2 extraction (metabolic) rates ranging from 1 to 5 ml O_2/100 ml blood. For comparison, the O_2 extraction for cerebral gray matter is approximately 8 ml O_2/100 ml blood using the mean cerebral O_2 consumption of 4 ml O_2/100 g tissue given in the *Biological Handbook*, and gray matter blood flow of 0.5 ml blood/ml tissue/min given by Albano & Columba (1976).

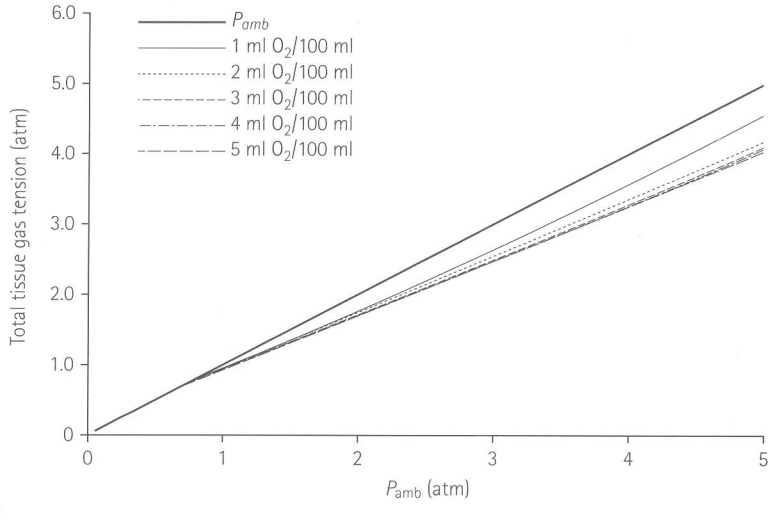

(a)

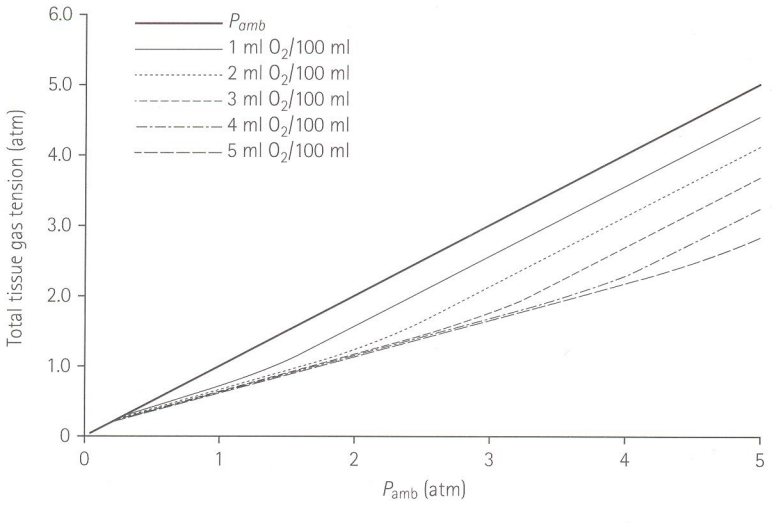

(b)

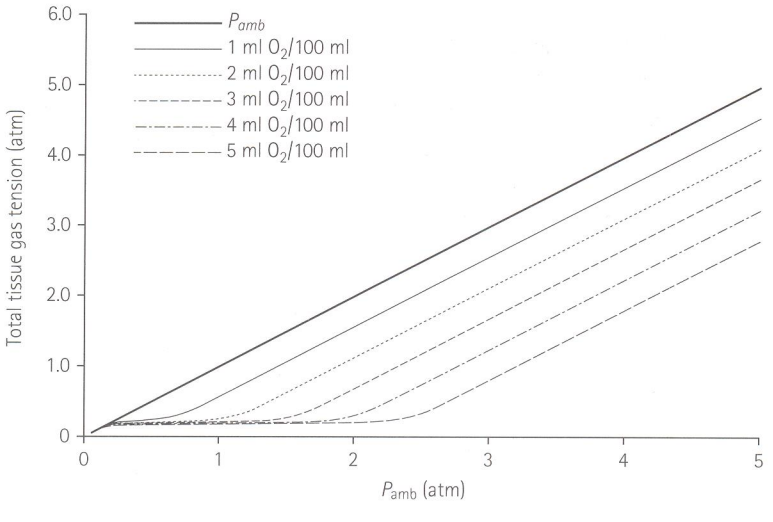

(c)

Fig. 10.1.7 Total tissue gas tensions at steady-state as functions of ambient pressure (atm) at various tissue O_2 extraction rates breathing: (a) air; (b) a 50% O_2-inert gas mix, and (c) 100% O_2. The oxygen window at a given P_{amb} is the difference between P_{amb} (the diagonal line in each panel) and the indicated total gas tension.

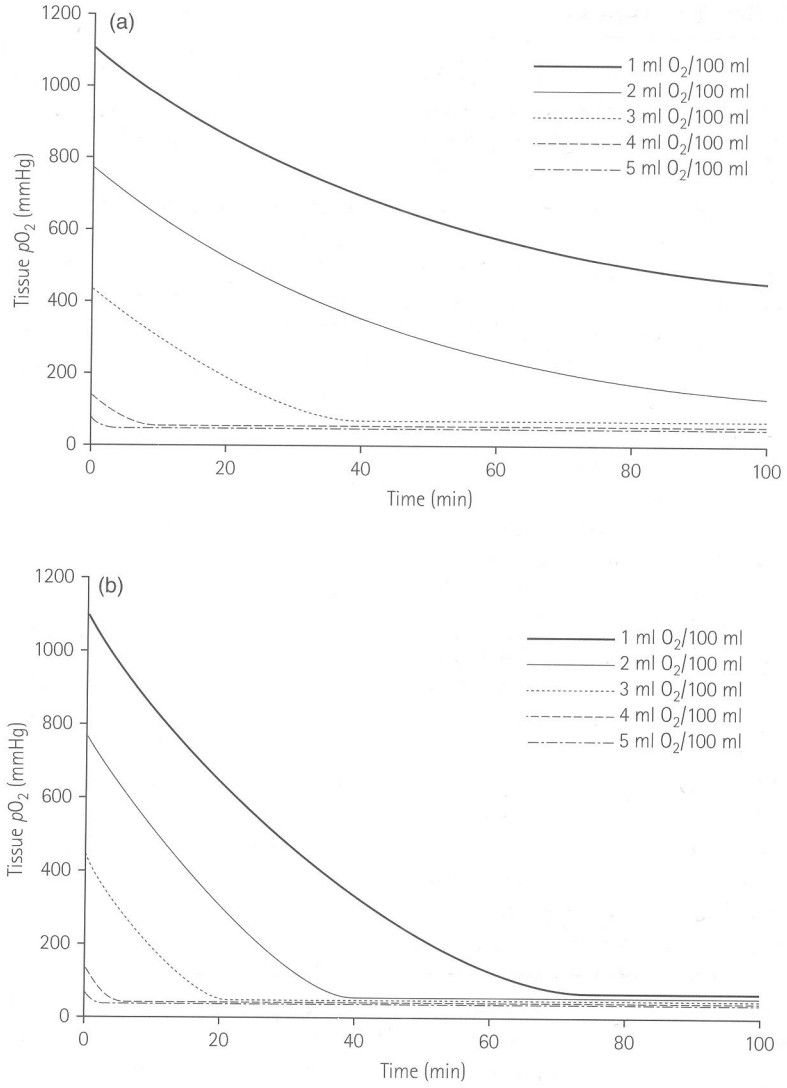

Fig. 10.1.8 Hypothetical p_{O2} in a 50 min time constant tissue as a function of time at 101 kPa (1.0 ATA) after an instantaneous decompression from steady-state breathing of 100% O_2 at 202 kPa (2.0 ATA). (a): 100% O_2 breathing continued after surfacing; (b): air breathing after decompression. Traces from top to bottom in each panel are for increasing tissue metabolic rates causing tissue O_2 extraction rates of 1, 2, 3, 4, and 5 ml/100 ml blood/min, respectively. Tissue O_2 solubility was assumed equal to plasma O_2 solubility.

shortening the transient tissue O_2 oversaturations that follow decompression.

The oxygen window is often exploited in modern decompression practice by increasing the O_2 partial pressure in inspired gas before and during decompression. For example, 100% O_2 is commonly breathed prior to decompressions from sea level saturation to altitude in order to widen the O_2 window, reduce the gas supersaturations incurred during the decompressions, and thereby reduce the risk of DCS while at altitude. Factors that increase $\dot{Q}$ and $c_{a\bar{v}O2}$ increase the rate of gas exchange during such O_2 prebreathes and reduce the times required to reduce given risk levels of DCS. Exercise is one such factor that has been successfully exploited to shorten O_2 prebreathe protocols for extravehicular activity (EVA) from the Shuttle and Space Station. Increases in the width of the O_2 window with ambient pressure also motivate breathing gas mixtures with high P_{O2} before diving decompressions, but this practice is limited by the increased attendant risks of pulmonary and CNS O_2 toxicity (Ch. 10.2).

DIFFUSION-LIMITED GAS EXCHANGE

It is readily envisioned that DCS involves poorly perfused tissues where the intercapillary distances are significant with respect to the diffusion of gas through the tissue. In such tissues, diffusion might limit the rate of blood–tissue gas exchange. The above treatments can approximate the overall impact of such diffusion limitation by relaxing the $p_{t,g} = p_{v,g}$ assumption invoked to obtain Equation 7. However, more rigorous alternative approaches to the solution of Equation 5, in which the well-stirred assumption of uniform gas tension in the tissue is relaxed, have been undertaken by many workers to explicitly consider the impact of diffusion limitation on gas exchange. One approach in which blood was assumed to equilibrate with tissue across a planar interface yielded the well-known 'square root time' relationship for the time required for a tissue to absorb or eliminate a given amount of inert gas (Hempleman 1969). Wienke (1989) provides a detailed review of this and other treatments of diffusion-limited gas exchange, and of blood–tissue gas exchange in general.

Diffusion-limited gas exchange has also been approximated using a serial perfusion model. The Kidd-Stubbs model (Kidd & Stubbs 1969), on which the DCIEM Diving Tables (DCIEM Diving Manual Part 2 1995) are based, is an arrangement of four compartments in series each having the same time constant. In the context of the m-parallel compartment generalization in Fig. 10.1.4, this model considers only a single compartment that is further divided into four subcompartments. While the subcompartment in contact with the blood supply receives gas first, the kinetics of gas uptake and elimination in the other subcompartments are interdependent in a complex fashion that approximates the gas diffusion process (Hennessey 1973). Model success in application to a wide range of dive conditions is consistent with the notion that gas diffusion may be an important factor in the etiology of DCS (Hills 1977). Regardless of whether gas exchange in tissues involved in DCS is limited by perfusion or diffusion, practical mathematical treatments of the two cases are nearly identical. In one case, a series of exponentials associated with different tissues is involved, while in the other, a series of exponentials associated with a single tissue is involved.

BUBBLE EVOLUTION

As indicated in Fig. 10.1.1, one or more bubbles may form and grow in a gas-supersaturated tissue to relieve gas supersaturation. This event is thought to trigger a host of secondary events (via biophysical and/or biochemical processes) that in turn can result in DCS. As also illustrated, however, the gas supersaturation may be relieved by 'physiologic' elimination via the circulatory and respiratory avenues. Which route the excess gas takes is largely determined by how bubbles evolve in the tissue. The following sections delineate the factors that govern bubble evolution.

CRITICAL RADIUS

The liquid state of tissue predestines an inherent instability to any mass of undissolved gas in the tissue. Mechanical equilibrium between a bubble and its surroundings is governed by the LaPlace equation:

$$P_b = \Sigma P_{b,g} + \Sigma P_{b,fix} = P_{amb} + \frac{2\gamma}{R} + \delta, \qquad (13)$$

where the subscript 'b' refers to the bubble, γ is the surface tension of the bubble liquid–gas interface, R is the bubble radius, and δ is any additional mechanical deformation pressure opposing bubble expansion. In the case of a flat liquid–gas interface, as shown in Fig. 10.1.2, the radius of curvature is infinite and δ is the external pressure. Most importantly, the bubble gas pressures must equal the dissolved gas tensions under the equilibrium presumed by Equation 13. Consequently, Equation 13 reveals that the liquid must be gas supersaturated for all $R > 0$: $\Sigma p_{t,g} + \Sigma p_{fix} - P_{amb} = P_{ss} = \frac{2\gamma}{R} + \delta$. Note that this level of gas supersaturation must increase as the bubble radius decreases

Under the assumption that water vapor, CO_2, and O_2 are 'fixed' components of tissue gas tension, $\Sigma p_{t,fix}$, and in constant equilibrium with the gas phase (i.e. $\Sigma p_{t,fix} = \Sigma P_{b,fix}$), the dependence of bubble pressure on bubble size is primarily dependent on the inert gas pressure as illustrated in Fig. 10.1.9. The inert gas pressure within the bubble (determined by Equation 13) exceeds the ambient pressure, in this example, when the bubble radius is less than 7 μm for P_{amb} = 101 kPa (1.0 ATA) and less than 4 μm for P_{amb} = 1013 kPa (10.0 ATA). Thus, a condition of gas supersaturation must exist for the existence of a bubble at sizes less than these radii. Also, at these ambient pressures, the inert gas pressure within the bubble asymptotically approaches (i.e. for infinitely large bubble radii or essentially flat interfaces) 0.19 and 0.37 atm below the ambient pressure, or 81 and 963 kPa (0.81 and 9.63 ATA), respectively, due to the presence of the fixed components. Bubble growth can only occur with a net transfer of gas into the bubble. Gas will transfer into the bubble if the gas tension outside the bubble exceeds

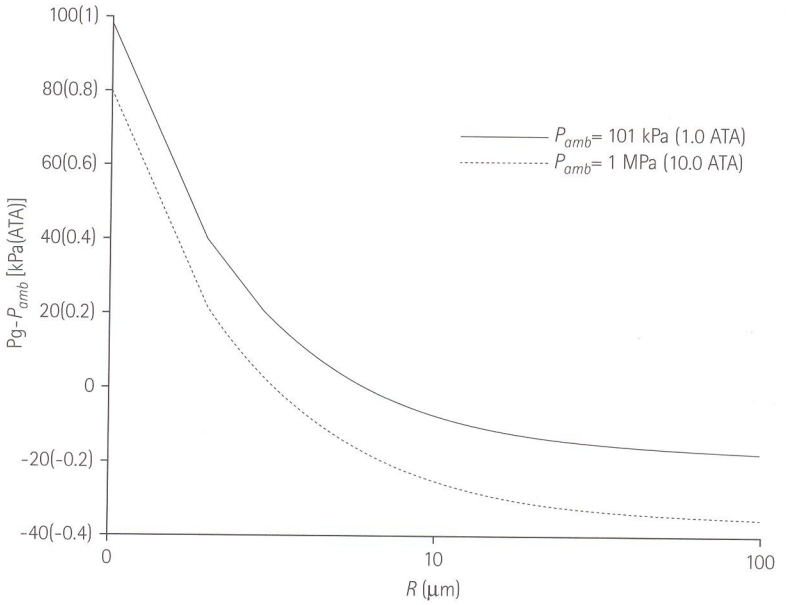

Fig. 10.1.9 Difference between the inert gas and ambient pressures for a bubble in equilibrium in tissue based on a balance of forces (Equation 13). Surface tension is 60 ergs/cm and the deformation pressure is ignored.

the gas partial pressure inside the bubble, i.e. if $\Sigma p_{t,g} > \Sigma P_{b,g}$. The asymptotic inert gas tensions of 81 and 963 kPa (0.81 and 9.63 ATA), in the above example, thus represent the minimum inert gas tension requirements for bubble growth. Increased curvature of the bubble surface (i.e. decreasing R) elevates the gas tension requirements for bubble growth.

The minimum requirements, however, exceed the normal saturation levels of N_2 tissue tension. At surface (100 kPa, 1.0 ATA) for example, the saturated N_2 tissue tension is 75 kPa (0.75 ATA). Since this value is less than the minimum required for bubble growth [81 kPa (0.81 ATA)], growth cannot occur until the ambient pressure is reduced by at least the difference between these two values or 6 kPa (0.06 ATA). At higher ambient pressures, the difference between the saturated N_2 tissue tension and the minimum required for bubble growth increases [e.g. 177 kPa (1.77 ATA at P_{amb} = 1 MPa (10 ATA)].

The minimum conditions for bubble growth lead naturally to the concept of the critical radius, R_c. The critical radius is a property of the liquid phase (Ward et al 1970). Its value is obtained by direct substitution of dissolved gas tensions for bubble partial pressures in Equation 13, then solving for R while ignoring δ to yield:

$$R_c = \frac{2\gamma}{\Sigma p_{t,g} - P_{amb}} = \frac{2\gamma}{P_{ss}}. \qquad (14)$$

Fig. 10.1.10 illustrates how R_c (right axis) varies during a standard air dive (DCIEM Diving Manual 1995) in a tissue compartment with a nitrogen time constant of 60 min. According to Equation 14, R_c is negative when the total gas tension is less than the ambient pressure; i.e., when $\Sigma p_{t,g} + \Sigma p_{t,fix} < P_{amb}$. An actual bubble under these conditions, however, has a positive radius and, according to Equation 13, an internal pressure greater than P_{amb}, and therefore the bubble must dissolve. In the example shown in Fig. 10.1.10, bubble growth can only occur after decompression is initiated, and only if the bubble radius exceeds R_c when its value is positive. Comparison of Equations 13 and 14 under this growth condition reveals that the total gas tension must exceed the total gas pressure within the bubble. The lowest positive value of R_c (~ 2 μm) occurs immediately after arrival at surface (at 38 min), when the gas supersaturation is maximal. R_c then increases (as N_2 tension decreases) to an infinitely large value at 187 min, when it transforms to an infinitely negative value. Thereafter, no bubble growth is possible as R_c increases to asymptotically approach the predive value of –21.6 μm. The transition of R_c from negative to positive values that occurs at the start of decompression is caused by the reversal in the gas tension–ambient pressure relationship.

The stability of a gas-supersaturated liquid is illuminated by considering the free energy of bubble formation. This free energy is given in the vicinity of the critical radius by (Ward et al 1970):

$$W_{rev} = \frac{4\pi\gamma \cdot R^2}{3}. \qquad (15)$$

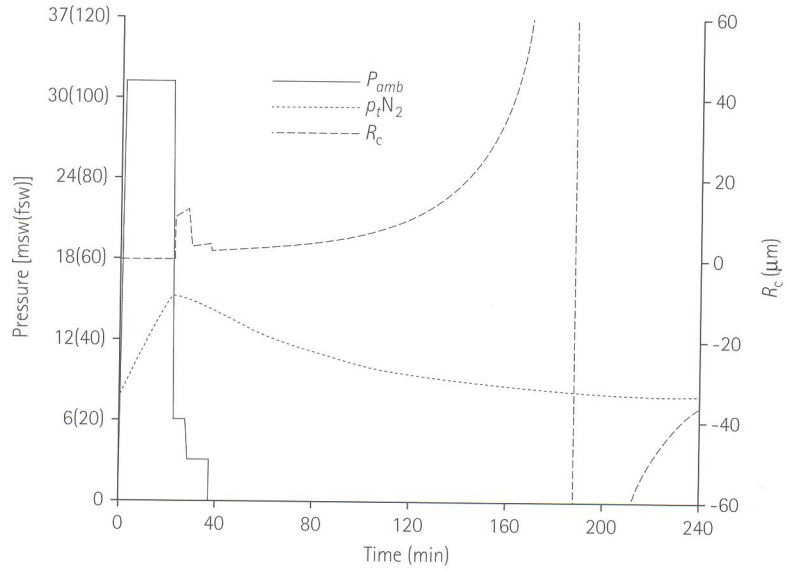

Fig. 10.1.10 Tissue N_2 tension (in msw absolute) and critical radius in a 60 min time constant compartment during a standard air decompression dive to 32 msw (104 fsw)/22 min. Surface tension is 60 ergs/cm^2 and the deformation pressure is ignored.

Plots of the free energy of bubble formation as a function of bubble radius, R, for two different gas supersaturations in water are illustrated in Fig. 10.1.11. In each case, the maximum free energy change is associated with formation of a bubble of size equal to the critical radius. By definition, the condition at $R = R_c$ is an equilibrium condition, but because any perturbation of R from the critical radius occurs with a decrease in free energy, the equilibrium is unstable (Tucker & Ward 1975a). With a decrease in R from R_c, the bubble dissolves with a decrease in free energy. With an increase in R from R_c, the bubble grows, unabated in a liquid of infinite extent. The unstable equilibrium at $R = R_c$ is called 'metastable.' A liquid will sustain the gas-supersaturated condition metastably until a fluctuation sufficient to generate a bubble of size greater than R_c occurs. Only then will such a bubble grow rather than collapse back into solution.

The metastable state at $R = R_c$ in Fig. 10.1.11 applies to a liquid of effectively infinite extent. If the region surrounding the bubble is sufficiently small so that the dissolved gas tension varies with bubble size (i.e. the absorption or release of gas by the bubble decreases or increases p), a second but stable state of equilibrium emerges at R greater than the illustrated R_c (Ward et al 1982b). In this case, a bubble of radius larger than R_c will converge towards the larger R of the stable state. The identification of this equilibrium state has helped explain the persistence of large populations of microbubbles in systems where each bubble is effectively constrained to exchange gas within a finite volume of fluid. The long term survival of such bubbles is still dependent on a condition of gas supersaturation, although the degree required is diminished when compared to an open volume system.

It should now be clear that bubbles in tissues, which we have seen are gas undersaturated throughout most of their existence, tend inexorably to dissolve, leaving tissue devoid of separated gas phase. Consequently, this suggests that bubble formation in tissue requires the de novo or spontaneous formation of surfaces of separation between liquid and gas. In principle, this initial event can be contemporaneous with the occurrence of gas supersaturation (when R_c is sufficiently positive) or can occur some time before decompression. In the latter case, some mechanism must stabilize the undissolved gas against dissolution, and thereby account for its persistence and availability to expand when gas supersaturation occurs.

BUBBLE FORMATION

Spontaneous or de novo bubble nucleation can occur homogeneously in the bulk of a liquid, where the material surrounding the event is spatially isotropic, or heterogeneously, proximate to a liquid–liquid or

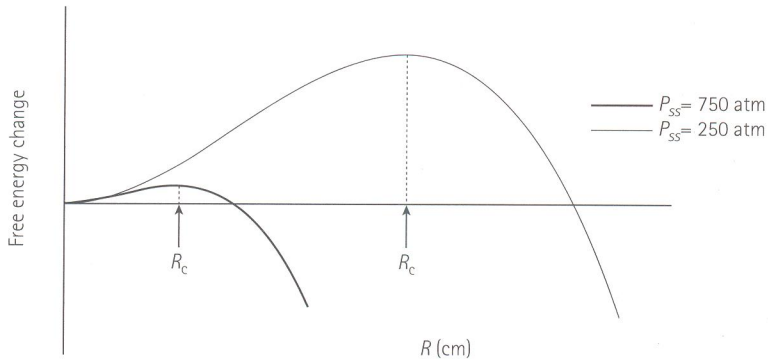

Fig. 10.1.11 Helmholtz free energy of bubbles in water with gas supersturations of 750 and 250 atm. An arrow indicates the critical radius in each case. The critical radius and corresponding free energy change decrease with increasing gas supersaturation, P_{ss}.

liquid–solid surface, where the material surrounding the event is spatially anisotropic.

Homogeneous Nucleation

The probability of homogeneous nucleation depends on the free energy of formation of a critical-sized bubble (Ward et al 1970):

$$P = Z \cdot exp(-W_{rev}/kT), \qquad (16)$$

where Z is the Zeldovich factor that embodies the influence of kinetic and inertial constraints, and W_{rev} is given by Equation 15. As illustrated in Fig. 10.1.11, W_{rev} increases with R_c and constitutes an energy barrier to the attainment of phase equilibrium in a gas-supersaturated liquid. The probability of homogeneous nucleation rapidly diminishes as R_c increases and becomes negligible at gas supersaturations typically encountered in diving or aerospace operations (Gerth & Hemmingsen 1976, Hemmingsen 1975).

The dependence of R_c on surface tension (Equation 14) and the appearance of R_c in the expression for W_{rev} in Equation 15 makes the probability of homogeneous nucleation at any given gas supersaturation extremely sensitive to the magnitude of the surface tension. In principle, homogeneous nucleation could occur at arbitrarily small gas supersaturations with sufficiently low values of the surface tension. It might be thought, therefore, that surface tensions in physiologic fluids may be sufficiently low by action of surfactants to account for homogeneous nucleation at the low gas supersaturations known to elicit DCS occurrence in man (Weathersby et al 1982). However, surface tension in the conventional sense is a macroscopic equilibrium property of a planar gas–liquid interface, which is actually a zone of thickness of molecular dimensions through which there is a continuous transition of properties characteristic of one phase to those of the other. During a spontaneous nucleation event, the gas–liquid interface is not at equilibrium and is ill defined. Once identifiable, it is of very small radius. On the basis of studies of the effects of surfactants on bubble nucleation in water gas supersaturated with argon by decompression from elevated pressures, Hemmingsen (1978) concluded that the adsorption of surfactants of molecular weight greater than about 330 dalton fails to occur at the gas–liquid interfaces of nascent bubbles fast enough to affect the spontaneous nucleation event.

It is important to differentiate bubbles that are primarily vaporous from those that are not. The former are bubbles that evolve when the ambient pressure is less than the vapor pressure of the liquid, such as occurs during boiling. Gas molecules in these bubbles essentially evaporate from the bubble interface. This process is limited only by heat transfer to the interface, and is hence relatively rapid with a high Zeldovich factor in Equation 16. On the other hand, bubbles that cause DCS form in liquids at hydrostatic pressures that are usually far above the vapor pressure of the surrounding liquid. Water vapor constitutes a smaller fraction of the contents of such bubbles as the ambient pressure–vapor pressure difference increases, so such bubbles must nucleate primarily from chance aggregation of (Foster et al 1998) gas molecules that diffuse some distance through tissue or blood, then across the bubble gas–liquid interface. Consequently, the nucleation and subsequent evolution of such bubbles is limited by the concentration and diffusivity of the dissolved gas, and is relatively slow with a low Zeldovich factor (Blander 1979, Finkelstein & Tamir 1985, Gerth 1979, Gerth & Hemmingsen

1976). Through the remainder of this chapter, decompression bubbles will be understood to be gaseous as opposed to vaporous in nature and the deformation pressure will be ignored unless stated otherwise (see Nims 1951 for a detailed examination of δ).

Heterogeneous Nucleation

Gas-supersaturation thresholds for homogeneous nucleation in bulk liquid are conditioned only by the nature of molecular interactions between the dissolved gas and liquid. In contrast, thresholds for heterogeneous nucleation are affected additionally by conditions unique to solid–liquid or liquid–liquid interfaces. The heterogeneity of tissue compels consideration of this type of nucleation in vivo.

Heterogeneous bubble nucleation at interfaces between aqueous and organic liquids should require lower gas supersaturations than homogeneous nucleation in either of the bulk liquids (Apfel 1971). Hills (1967) reported results of experiments in which bubbles were observed to form at the horizontal interface between water and paraffin oil when decompressed to subatmospheric pressures. However, these results could not be repeated when, in similar experiments (Evans & Walder 1969, Gerth 1979), the liquids and interfaces were first exposed to high hydrostatic pressure to extinguish any pre-existing gas nuclei (cf below).

Heterogeneous nucleation at any solid surface that is not perfectly wetted by the liquid is thermodynamically favored over homogeneous nucleation, although more severe kinetic constraints at such a surface conspire to mitigate the overall facilitative effect. Yount & Kunkle (1975) considered that a perfectly hydrophobic sphere might theoretically provide the ideal nucleus because a concentric shell of liquid vapor would always surround it. They concluded, however, that because the lower limit of the shell thickness must be the order of molecular dimensions, such spheres should not be effective in reducing gas supersaturations required for spontaneous bubble nucleation in liquids.

Empirical studies of heterogeneous nucleation at solid surfaces are difficult because solid surfaces at which nucleation should theoretically occur most favorably are also those most able to trap pre-existing nuclei. Gerth & Hemmingsen (1980) studied bubble nucleation at the surfaces of solids that had been crystallized in situ by cooling concentrated aqueous solutions before decompression, but after they had been N_2- or Ar-saturated at elevated pressures, thereby obviating the involvement of pre-existing nuclei. Prevailing gas supersaturations after decompression were corrected for the effects of cooling and crystallization. Bubbles were observed to nucleate at the surfaces of some of the organic crystals studied at gas supersaturations less than 10 atm, motivating the conclusion that heterogeneous nucleation at certain solid–liquid interfaces may account for the origin of bubbles observed at relatively low apparent gas supersaturations in vivo.

Pre-Existing Gas Nuclei

If a bubble already exists when liquid or tissue becomes gas supersaturated, that bubble can grow once its radius exceeds the critical radius of the liquid. Because such growth occurs from a non-zero initial radius, it circumvents that portion of the energy barrier associated with de novo formation from zero radius to the initial radius, and allows macroscopic bubbles to appear at gas supersaturations that are potentially far less than those required for de novo nucleation. Such persistent bodies of undissolved gas are called 'pre-existing' gas nuclei. A large body of evidence indicates that many tissues contain a nearly ever-present population of such nuclei (Vann 1989). This evidence must be reconciled with the fact that tissues under normobaric conditions have negative critical radii (see Fig. 10.1.10 at $t = 0$). Mechanisms must therefore exist to stabilize gas nuclei against dissolution under normobaric and hyperbaric conditions to explain the persistence of such nuclei.

Various stabilization mechanisms for bubbles in unsaturated tissue/blood have been proposed based on the presumption that surface active materials adsorb to the gas–liquid interface and allow the interface to support a negative pressure, thereby preventing bubble dissolution (Fox & Herzfeld 1954, Van Liew & Burkard 1995, Van Liew & Raychaudhuri 1997, Yount 1979a). The various mechanisms differ in their assumptions about the gas permeability of the adsorbed layer and in details of how mechanical–chemical properties of this layer vary with surface area or nucleus size. Described below are two gas nuclei stabilization mechanisms, one involving adsorption of surface active molecules and the other involving geometrical factors.

Varying Permeability Model

Yount (1997, 1979a, 1982) introduced the varying permeability model (VPM) where bubble nuclei are assumed to be stabilized against extinction by skins of adsorbed amphiphilic molecules, and have an integral distribution of sizes given by:

$$N = N_o \, exp\left(-\frac{R_{min}}{\beta}\right), \tag{17}$$

where N is the number of nuclei of radius greater than or equal to R_{min}, N_o is the constant overall number of

nuclei, and β is a slope factor. The smallest nuclei that can be recruited from the distribution at supersaturation P_{SS} has a radius given by:

$$R_{min} = 2\gamma/P_{ss} = R_c. \quad (18)$$

Substitution of Equation 18 into Equation 17 gives the number of bubbles nucleated (or recruited) at P_{ss}:

$$N = N_o \, exp\left(-\frac{2\gamma}{P_{ss} \cdot \beta}\right). \quad (19)$$

The distribution of nuclear sizes is assumed to be affected by pressure, under the constraints that:

1 no nuclei are extinguished by any overpressures; and
2 the original ordering of nuclear sizes is always preserved.

Under these constraints, the number of nuclei, $N(R_{min})$, of radii greater than or equal to r_{min} after exposure to a maximum overpressure,

$$P_{crush} = MAX\,[P_{amb} - (\Sigma p_t - \Sigma p_{fix})], \quad (20)$$

must equal the number of nuclei, $N(R^o_{min})$, of radii greater than or equal to R^o_{min} in the distribution of nuclei present before the exposure. Applying Equation 17:

$$N = N_o \, exp\left(-\frac{R_{min}}{\beta}\right) = N_0 \, exp\left(-\frac{R^o_{min}}{\beta^o}\right), \quad (21)$$

where β^o is the slope factor for the initial nuclear size distribution. If the adsorbed skins on the nuclei are assumed to remain always permeable to dissolved gases, the gas supersaturation required to nucleate the N bubbles in Equation 21 then depends on P_{crush} (Yount 1979a):

$$P_{ss} = \frac{2\gamma(\gamma_c - \gamma)}{\gamma_c \, r^o_{min}} + P_{crush}\left(-\frac{\gamma}{\gamma_c}\right), \quad (22)$$

where γ_c ($> \gamma$) is the 'crumbling compression' that counters the tendency for surface tension to extinguish small bubbles (*cf* Fig. 10.1.12). The slope factor β for the distribution at a given pressure is then obtained from Equations 18, 21, and 22:

$$\beta = \beta^o\left(\frac{R_{min}}{R^o_{min}}\right) = \frac{2\gamma_c\beta^o}{2(\gamma_c - \gamma) + P_{crush}R^o_{min}}. \quad (23)$$

The effect of P_{crush} on all nuclei in the initial distribution is given in terms of a specific portion of the distribution; i.e. only those nuclei with radius R^o_{min}.

The nucleus of largest size in the distribution governs the inception of bubble formation. This nucleus has a radius, R_{max}, given by Equation 17 with $N = 1$ and β from Equation 23 using the maximum overpressure achieved in the profile up to the time of interest:

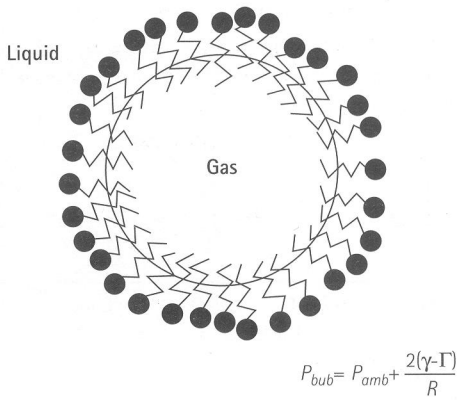

Fig. 10.1.12 By virtue of a spreading compression, Γ, exerted by an adsorbed film of surface-active agents at the gas–liquid interface, the effective surface tension, $(\gamma - \Gamma)$, is reduced, enhancing bubble stability. For small changes in bubble radius, Γ varies with interfacial area and assumes a maximum value called the 'crumbling compression,' γ_c, when the bubble area is reduced to the point where surfactant molecules begin to be 'squeezed out' of the interface.

$$R_{max} = \beta ln\,(N_o). \quad (24)$$

It follows from Equation 23 and the definition of P_{crush} that under initial conditions where $\beta = \beta^o$, $R_{max} = R^o_{max}$ corresponds to an overpressure, P^o_{crush}, given by:

$$P^o_{crush} = \frac{2\gamma}{R^o_{max}}, \quad (25)$$

which defines a minimum overpressure that must be attained before the distribution can be affected by pressure. Increasing compartmental overpressures in excess of P^o_{crush} decrease β and shift the population of nuclei towards smaller sizes.

Gas supersaturations of magnitude smaller than required to recruit a nucleus of radius R_{max} are sustained metastably; i.e. without bubble formation. Larger gas supersaturations are accompanied by bubble nucleation and growth from increasing numbers of nuclei recruited according to Equation 19. Exposure to $P_{crush} > P^o_{crush}$ consequently increases the threshold gas supersaturation for bubble inception and reduces the number of nuclei recruited to become macroscopic bubbles at supersaturations larger than this threshold. This behavior is illustrated in Fig. 10.1.13.

The ability of adsorbent molecules to be 'squeezed out' of the layer with sufficient compression as the nucleus diminishes in size is a central feature of the VPM. This behavior is in accord with that observed in other physiologic liquid–gas systems (Otis et al 1994) and allows gas nuclei to be crushed to smaller stable

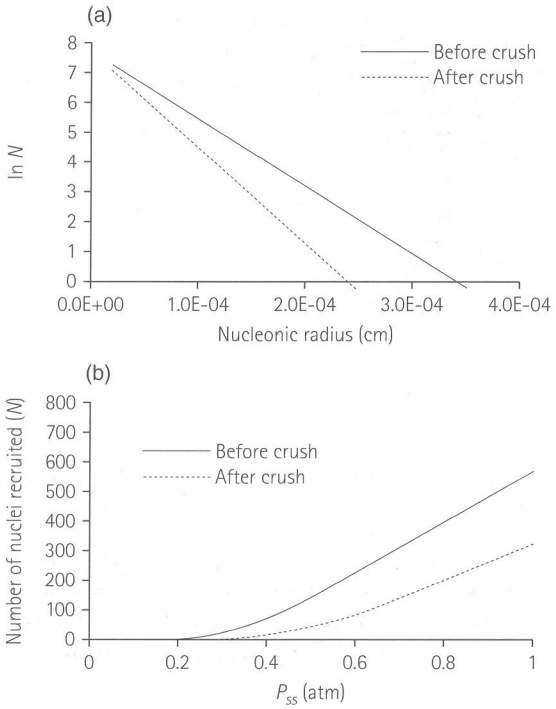

Fig. 10.1.13 Graphical representations of the size distribution of pre-existing bubble nuclei in a compartment (a) and the corresponding number of bubbles recruited to grow as the compartment supersaturation, P_{ss} increases and effects of nucleus recruitment and growth on P_{ss} are neglected (b). Note that bubble growth depletes the prevailing supersaturation, so that growth of increasing numbers of recruited nuclei increasingly limits the supersaturation attained during decompression. Increasing values of N in the illustrated distribution consequently become ever more difficult to realize.

sizes without extincting them. Van Liew & Raychaudhuri (1997), on the other hand, developed a model of gas nuclei stabilized by absorbed layers that are unable to change content with compression. Such nuclei cannot be crushed to stable smaller sizes, but collapse to extinction when compressed to less than a limiting minimum size.

Crevice Model

Another stabilization mechanism involves the entrapment of gas nuclei within hydrophobic crevices on the surfaces of solid or semi-solid materials in contact with the liquid (Harvey 1951). As illustrated in Fig. 10.1.14, the gas–liquid interface in such crevices has a negative radius of curvature (surface concave towards the liquid phase) so that the LaPlace surface tension acts increasingly against the liquid with increased penetration, thus stabilizing gas nuclei in undersaturated gas–liquid solutions. In fact, vaporous nuclei form spontaneously under such conditions within a crevice if the receding contact angle is sufficiently large, i.e., $\alpha_R \geq 90° + \phi$ (Harvey et al 1944).

Other plausible crevice geometries, such as the elliptical crevice illustrated in (b) of Fig. 10.1.14, allow for an inversion of the gas surface and with further penetration of the nucleus into the crevice, the opposing LaPlace pressure against the liquid increases markedly (i.e. $2\gamma/R \rightarrow -\infty$) (Tikuisis 1986). Hence, a gas phase contained within such a crevice can be supported indefinitely under conditions of undersaturation or negative critical radii under the less restrictive condition that the receding angle $\geq 90°$. This mechanism successfully explained the observations of decompression bubbles in crustaceans that underwent various pressure-decompression profiles (Daniels et al 1984).

Hydrodynamic and Mechanical Facilitation

Nucleation by any of the mechanisms described above can be facilitated at relatively low apparent gas supersaturations by hydrodynamic or mechanical effects that decrease the hydrostatic pressure and increase the prevailing gas supersaturation in small, localized regions of tissue. These effects may even be sufficient to produce transient negative pressures or tensions that cause formation of bubble nuclei in macroscopically gas-undersaturated tissue. The nuclei may coalesce into larger nuclei (Yount 1983) that are recruited to grow at the then-prevailing gas supersaturation, or become stabilized by one of the mechanisms described above to persist until recruited to grow with later occurrence of a suitable gas supersaturation. For example, Hennessy (1989) has proposed that arterial microbubbles, nucleated primarily in circulatory turbulence at the tips of the cusps of the pulmonary valve, are the primary cause of the common forms of DCS, although other mechanical effects (e.g. ultrasound, tribonucleation, radiation) must also be considered.

Doppler shifts of reflected incident ultrasound at relatively low power is routinely used to detect moving bubbles in the circulation (Nishi 1993). Ultrasonic imaging is also used in many laboratories to visualize both moving and stationary bubbles in tissue. However, acoustic radiation of sufficient power can also produce sufficient transient tensions in the liquids of tissue to cause spontaneous nucleation of bubbles, while rectified diffusion (Fyrillas & Szeri 1994) can promote growth of nascent bubble nuclei to critical size and facilitate bubble nucleation (Crum & Hansen 1982, Crum & Mao 1996, Crum et al 1987, Dalecki et al 1997).

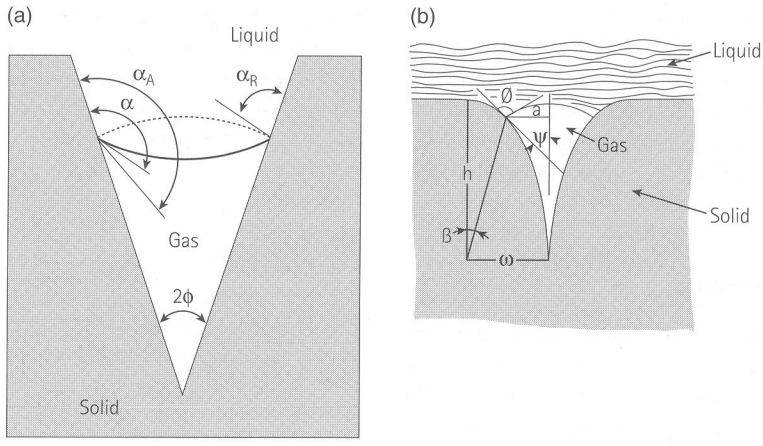

Fig. 10.1.14 Gas nucleus stabilized in (a) a conical crevice and (b) an elliptical crevice on the surface of a hydrophobic solid in a gas-undersaturated liquid. The dotted line in (a) indicates the configuration of the interface at the point where it will begin to recede from the apex of the crevice in a sufficiently gas-supersaturated liquid. 2ϕ is the apex angle of the crevice. α_A is the advancing angle of contact between the gas–liquid interface and the crevice wall at which the interface advances along the unwetted crevice wall. α_R is the receding angle of contact between the gas–liquid interface and the crevice wall at which the interface recedes along the previously wetted crevice wall. The interface remains stationary for all contact angles, α, that satisfy: $\alpha_A > \alpha > \alpha_R$. In (b), h and a are the crevice height and width, respectively, ϕ is the receding contact angle, and ψ is angle between the central (vertical) axis and the tangent to the gas–liquid interface.

By virtue of viscous adhesion between liquid and solid, liquid between separating or moving solid surfaces is under transient tensile stress that reduces its hydrostatic pressure. A classic example of such a condition in vitro occurs in the liquid region behind the moving point of contact between a liquid-immersed sphere and a solid surface upon which the sphere is made to roll (Ikels 1970). The increased critical radius of the affected liquid then promotes bubble nucleation, potentially aided by accompanying transient changes in vicinal properties of the solid–liquid interfaces involved. This process, called tribonucleation (Hayward 1967), plausibly accounts for observations of in vivo bubble formation that accompanies joint flexion and motion in otherwise bubble-free gas-supersaturated invertebrates (Evans & Walder 1969, McDonough & Hemmingsen 1984a,b), and for the well-known increase in DCS susceptibility in man associated with performance of exercise after decompression (Kumar & Powell 1994, Van der Aue et al 1949).

Tribonucleation can also generate vapor bubbles that acquire sufficient amounts of inert gas to delay their collapse back into solution when the opposing crushing pressure returns. The nuclei may then become stabilized by coalescing into larger more stable bubbles; a process facilitated by any local turbulence, by adsorbing surface active material, or by associating with solids in the liquid. Thus, normal day-to-day ambulation and exercise is thought to produce populations of nuclei that persist as the product of a dynamic equilibrium between nuclei production and dissolution (Vann et al 1989). Vann and coworkers (Vann, 1989; Vann & Thalmann 1993; Vann et al 1989) provide extensive reviews of possible sources of vaporous cavitation leading to decompression bubbles.

High-energy ionizing particles, such as neutrons in cosmic radiation or alpha particles from radioactive decay of U238 incorporated in the matrix of bone (Walder & Evans, 1974), deposit energy as they travel through tissue, producing a train of thermal spikes that can rupture with the formation of vapor-filled microcavities. The coalescence of a train of microcavities formed along a segment of the particle path length longer than the final diameter of the resulting bubble may be involved (Sette 1967, Sette & Wanderlingh 1967).

BUBBLE GROWTH

Once a bubble has nucleated; i.e. attained a size equal to or greater than the critical radius; its contents and size will change according to the prevailing difference between the dissolved gas tension and the bubble gas pressure at the gas–liquid interface. Of course, water vapor is assumed to be always in equilibrium between bubble and tissue. The metabolic gases, O_2 and CO_2,

are also often included with water vapor in this equilibrium assumption, so that $\Sigma P_{b,fix} = \Sigma p_{fix}$ at the gas–liquid interface. Adopting this assumption except where otherwise noted, we first summarize the quantitative expressions for the changes in bubble contents and size that are obtained when only a single inert gas is involved.

Single Inert Gas Dynamics

If the inert gas is assumed to be always in equilibrium between the bubble and a well-perfused tissue, the gas tension in the tissue equals its partial pressure in the bubble, and both are coupled to the ambient pressure by the LaPlace equation (Equation 13). Thus, if surface tension and mechanical effects are neglected, then $p_{t,g} = P_{b,g} = P_{amb} - \Sigma p_{fix}$. The rate of change of bubble volume is then obtained from the expression for mass balance between the bubble, tissue, and blood, which is given for a perfusion-limited system by Equation 10 with addition and appropriate elaboration of the $-Z_b$ term (Equation 6):

$$\frac{dp_{t,g}}{dt} = \frac{m_{a,g} \cdot t + (p^o_{a,g} - p_{t,g})}{\tau} - \left(\frac{1}{a_{t,g}V_t}\right) \cdot \left(\frac{d(P_{b,g}V_b)}{dt}\right), \quad (26)$$

where $kTP_{b,g}V_b$ is the number of moles of gas g at partial pressure $P_{b,g}$ in a bubble of volume V_b. Under the equilibrium conditions stipulated above, Equation 26 is solved to obtain the following expression for the rate of change of bubble volume at constant ambient pressure and $p_{a,g}$ (Vann 1982):

$$\left(\frac{dV_b}{dt}\right) = \alpha_{blood,g}\dot{Q} \cdot \left(\frac{p_{a,g}}{p_{t,g}} - 1\right). \quad (27)$$

Equation 27 is readily shown to imply that the bubble volume must decrease monotonically during any isobaric stage after decompression.

When the attainment of equilibrium between bubble and tissue is limited by diffusion, the flux of a given gas across the gas–liquid interface is governed by the Fick-Fourier diffusion equation:

$$\frac{d}{dt}(P_{b,g}V_b) = kTAD \cdot \left.\frac{\partial c}{\partial R}\right|_{R=R_i}, \quad (28)$$

where A is the surface area of the gas–liquid interface and R_i is the radius of the bubble where spherical symmetry is assumed. Again, solution of this equation for the rate of change of bubble volume is simplest when effects of surface tension, mechanical deformation, and changes in bubble surface area with bubble size are neglected. Under these conditions, Equation 28 implies that the flux and consequent rate of change of bubble volume at constant P_{amb} are proportional to the gas supersaturation. More comprehensive treatments relax the assumptions leading to this simple deduction.

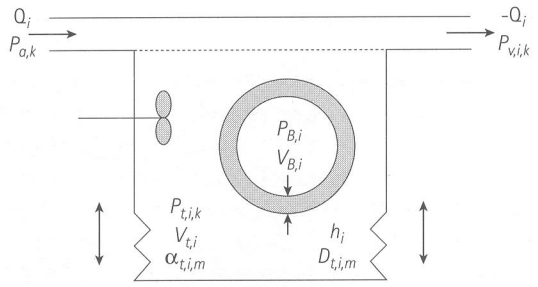

Fig. 10.1.15 Schematic of the three-region model, consisting of a gas bubble covered by an unstirred and unperfused boundary layer of constant and uniform thickness h within a well-stirred tissue mass.

Models that consider the gas bubble to be covered by an unstirred and unperfused boundary layer of constant and uniform thickness h within a well-stirred tissue mass are referred as three-region models (Fig. 10.1.15). Assuming spherical symmetry with the center of the bubble at $R = 0$, the diffusion equation for the $\partial c/\partial R$ factor in Equation 26 is:

$$\frac{\partial c}{\partial t} = D\left[\frac{\partial^2 c}{\partial R^2} + \frac{2}{R}\frac{\partial c}{\partial R}\right]. \quad (29)$$

Under the quasistatic assumption, $\partial c/\partial t$ is neglected and, with boundary conditions $c(R_i,t) = c_i$ at the bubble surface and $c(R_o,t) = c_o$ at the outer surface of the boundary layer, the solution of Equation 29 at the bubble surface is:

$$\left.\frac{\partial c}{\partial R}\right|_{R=R_i} = (c_o - c_i) \cdot \left(\frac{1}{h} + \frac{1}{R_i}\right). \quad (30)$$

For large R_i, Equation 30 reduces to:

$$\left.\frac{\partial c}{\partial R}\right|_{R=R_i} = (c_o - c_i) \cdot \left(\frac{1}{h}\right), \quad (31)$$

and divergence of the gas tension gradient in the vicinity of the bubble vanishes. Substitution of Equation 31 into Equation 28 yields (Tikuisis et al 1983, 1994):

$$\frac{dR}{dt} = \frac{D \cdot \alpha_{t,g} \cdot (p_{t,g} - P_{b,g})/h - (R/3) \cdot \left(\frac{dP_{amb}}{dt}\right)}{P_{amb} - \Sigma P_{fix} + 4\gamma/3R}. \quad (32)$$

Note that with no gas flux across the bubble boundary (i.e. $p_{t,g} = P_{b,g}$), Equation 32 reduces to the expression

for Boyle's law effects on bubble size. When the influence of tissue elastic deformation is considered, an additional term, $8\partial R^3\varepsilon/3$, appears in the denominator, where ε is the tissue modulus of elasticity (Gernhardt 1991). While the rate of bubble dissolution increases as $R \rightarrow 0$, unconstrained bubble growth asymptotically approaches a finite value as $R \rightarrow \infty$, provided the inert gas tension is unaffected by the growth of the bubble.

Equation 31 is inappropriate for small bubbles due to the neglect of the divergence of the gas tension gradient. This deficiency is remedied through the substitution of Equation 30 instead of Equation 31 into Equation 28, which ultimately yields:

$$\frac{dR}{dt} = \frac{D \cdot \alpha_{t,g} \cdot (p_{t,g} - P_{b,g}) \cdot (1/R + 1/h) - (R/3) \cdot \left(\frac{dP_{amb}}{dt}\right)}{P_{amb} - \Sigma P_{fix} + 4\gamma/3R}. \quad (33)$$

The additional $1/R$ term in the numerator was shown to have a significant impact on the maximum bubble volume attained after a given decompression (Srinivasan et al 1999). For bubble evolution in small finite volumes, additional analytic provisions must be made to vary the gas contents of the diffusion layer in accord with Henry's law (Srinivasan et al 2000).

Tikuisis et al (1983) solved the three-region problem with a variable bubble boundary thickness that disappears as $R \rightarrow 0$ and without the quasistationary approximation (i.e. where changes in gas concentration over time are ignored) used above. However, the more rigorous solution is rather cumbersome for modeling purposes. Tikuisis et al also relaxed the usual assumption of local equilibrium between gas and liquid at the gas–liquid interface, and used statistical rate theory as developed by Ward (1977) and applied to gas bubbles (Ward et al 1982a) to account for non-equilibrium effects on the transinterfacial gas flux. The flux of gas g across the bubble boundary is then given by:

$$J = K \cdot \left(\frac{p_{t,g}}{P_{b,g}} - \frac{P_{b,g}}{p_{t,g}}\right), \quad (34)$$

where K is the rate at which gas molecules contact available sites for absorption at the interface. The resultant non-equilibrium expression for bubble evolution in the three-region model at constant pressure is:

$$\frac{dR}{dt} = \frac{kT \cdot J}{P_{amb} - \Sigma P_{fix} + 4\gamma/3R}. \quad (35)$$

Van Liew & Hlastala, (1969) considered the region immediately surrounding the bubble to be uniformly perfused by adding the perfusion term from Equation 5 to Equation 29. They then converted concentrations to partial pressures, and infinitely expanded the region by solving the resultant expression under boundary conditions $p = P_b$ at $r = r_i$ and $p = p_a$ as $r \rightarrow \infty$, while neglecting effects of surface tension and changing hydrostatic pressure. In a more recent treatment of this two-region model, so named because it consists only of the bubble and the surrounding tissue, Srinivasan et al (1999) corrected these latter omissions and used the outer boundary condition $p = p_t$ as $r \rightarrow \infty$. The final expression for dR/dt is identical to the three-region model of Equation 33, except h in the second parenthesis on the left is replaced by $\sqrt{D\tau}$. The resultant dR/dt expressions in these versions of the two- and three-region models therefore differ only in their parameterizations.

Ward et al (1986) applied statistical rate theory to the two-region problem and derived the following expression for tissues at constant pressure:

$$\frac{dR}{dt} = \frac{D \cdot \alpha_{t,g} \cdot (p_{t,g} - P_{b,g}) \cdot (1/R + 1/\sqrt{\pi Dt})}{P_{amb} - \Sigma P_{fix} + 4\gamma/3R}, \quad (36)$$

which is similar to the two-region analog of Equation 33, except for the replacement of τ by πt in the $\sqrt{D\tau}$ term.

Hlastala & Van Liew (1975), and Meisel et al (1981) relaxed the quasistatic assumption to obtain complete solutions to the two-region problem under the boundary condition $p = p_a$ as $R \rightarrow \infty$. However, these solutions require p_a (or p_t) to be independent of both R and t, rendering them of limited utility in practical physiologic decompression problems.

Mass Balance in Finite Volumes

Each of the above models of bubble dynamics gives the rate of bubble evolution as a function of the tissue tension, $p_{t,i}$. In perfusion-limited systems, values of the latter for solution of the dR/dt functions are obtained from Equation 26. Note that if the tissue volume is infinite, as in the above two-region models, the second term on the right side of Equation 26 vanishes and the bubble fails to affect the value of $p_{t,g}$. Therefore, two-region models of bubble evolution are essentially single-bubble models that cannot be used to consider interactions between multiple bubbles. In contrast, as a bubble grows or dissolves in the finite tissue volumes of the three-region models, it exchanges gas with its surroundings, affecting the dissolved gas concentration and tension. These more realistic models reflect the fact that a growing bubble must deplete its surroundings of dissolved gas and relieve the local gas supersaturation. In the tissue–bubble equilibrium model that yields Equation 27 for the rate of bubble resolution, for example, the tissue gas tension is reduced immediately

to a value close to the ambient pressure ($P_{amb} - \Sigma p_{fix}$) when bubble formation occurs. This, in turn reduces the tissue–blood concentration gradient (Baz & Abdel-Khalik 1986, Kislyakov & Kopyltsov 1988), slows gas elimination from the tissue, and impacts the dynamics of other bubbles at sufficiently close proximity in the tissue (Gault et al 1995, Srinivasan et al 1999, 2000, Tikuisis & Nishi 1994, Tikuisis et al 1994, Van Liew & Burkard 1993) as illustrated in Fig. 10.1.16.

As the bubble number density increases, tissue gas tensions become clamped to the corresponding pressures of the gases in the bubble, which in a single gas system, is a function of ambient hydrostatic pressure only. Gas elimination from the finite tissue then follows slower time-linear kinetics until the bubbles are completely resolved. This slowing of bubble resolution and gas elimination from the tissue with increasing bubble number density is evident in (b) of Fig. 10.1.16. This behavior is also obtained with a single bubble if surface tension effects are neglected and the bubble is assumed always in equilibrium with the tissue, and is a central feature of the Exponential-Linear (EL) model to be described later.

The above treatments of the mass-balance problem in three-region models incorporate considerable simplification of the diffusion process, effectively collapsing all diffusion limitation into a factitious boundary layer or region around the bubble while leaving the remainder of the modeled tissue volume well-stirred (Srinivasan et al 2000). It is through bubble effects on the gas tensions in this well-stirred region that bubble–bubble interactions then occur. In a more rigorous treatment of the two-bubble problem, Jiang et al (1996) solved the diffusion equation for the overlapping diffusion regions of the two bubbles. These authors found that the lifetimes of the paired bubbles in close proximity are longer than when the bubbles are infinitely separated, but the difference quickly reduces with increasing separation; e.g. bubble lifetimes are less than 4% longer when more than 10 bubble diameters apart.

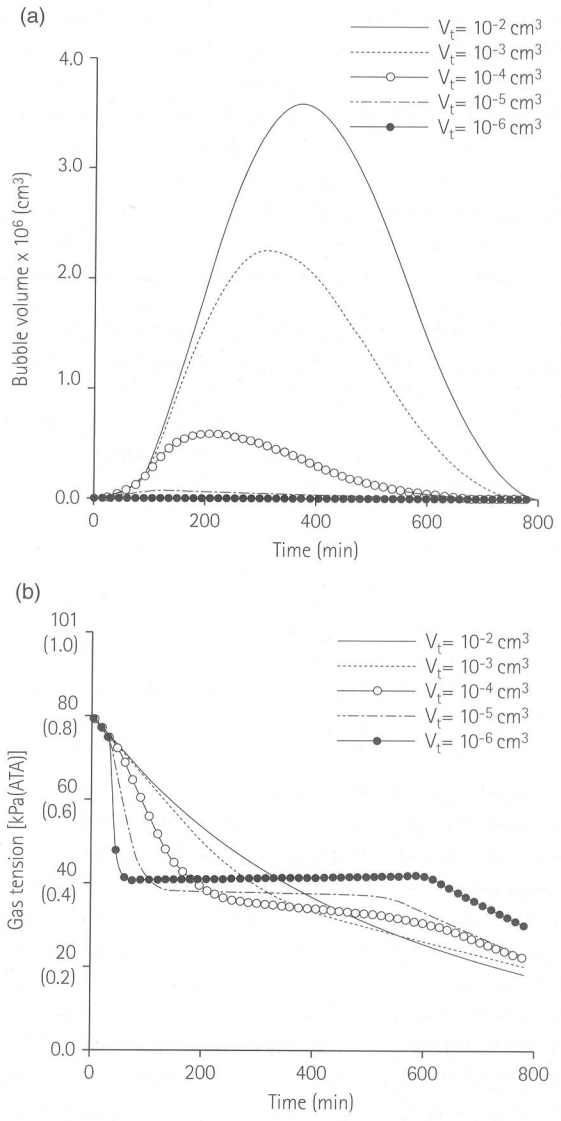

Fig. 10.1.16 Effect of tissue volume in the three-region model on bubble growth (a) and inert gas tension p_t in the well-stirred region (b) of a 360 min half-time tissue during a 30 min 100% oxygen prebreathe at sea level followed by a 5 min ascent to an indefinitely long exposure at 7620 m (25 000 ft) altitude. (From Srinivasan et al 1999)

Multigas Dynamics

The composition of the inspired inert gas is often changed in a pressure profile, requiring consideration of the simultaneous exchange of multiple inert gases between bubble, tissue, and blood. The above expressions for bubble evolution and tissue tension are readily elaborated to accommodate such problems by simply assuming that the fluxes of the m gases involved are independent of each other. In the two- and three-region bubble dynamics models, for example, the resultant dR/dt expressions resemble Equation 33, except that a sum of terms, one for each of the m gases, replaces the single term associated with gas g in the numerator of each expression (Srinivasan et al 1999). A more rigorous approach is to consider transfer of gas along a near-equilibrium path by applying the minimum rate of entropy production at the bubble boundary (Tucker & Ward 1975b). Again, an equation resembling Equation 35 is obtained, but the value of the summed gas

pressure, $\sum_{g}^{m} P_{b,g}$, in the the expression for J is adjusted.

Notably, accommodation of multiple inert gases under the assumption of equilibrium between bubble and tissue can be handled in at least two ways. In both, the sum of the tissue tensions is coupled to the ambient hydrostatic pressure through the sum of the bubble pressures, $\sum_{g}^{m} p_{t,g} = \sum_{g}^{m} P_{b,g}$ and the LaPlace equation (Equation 13). Term-by-term equivalence of these sums can then be presumed to obtain an analog of Equation 27 that consists of a sum of m terms. Parker et al (1998), however, relaxed this latter presumption and, still neglecting surface tension and mechanical effects, computed the individual $p_{t,g}$ for the solution of Equation 13 by rearranging the expression for the total tissue content of each gas:

$$n_g = \alpha_{t,g}\, p_{t,g} + \frac{p_{t,g} V_b}{kT} \tag{37}$$

to obtain:

$$p_{t,g} = \frac{n_g}{\alpha_{t,g} + V_b/kT}, \tag{38}$$

where the first term on the right side of Equation 37 is the amount of gas g in solution and the second term is the amount of undissolved gas g in one or more bubbles. Substitution of Equation 38 into Equation 13 (with $\gamma = 0$ and $\delta = 0$) and rearrangement yields a homogeneous polynomial of order m with positive real root equal to V_b/kT. This root (and V_b) is determined by standard methods, but because it is a function of n_g and $p_{t,g}$, it must be iterated over successive small intervals of time. This required resort to numerical methods contrasts with the simple analytic solution for V_b that is obtained in the single gas problem by the simple integration of Equation 27.

Bubble-Tissue Interactions

Once a gas bubble has formed, it begins to interact with its immediate surroundings. It is well known that bubbles initiate a variety of biochemical responses in addition to any physical trauma that their presence might cause. Several investigators have reported on the biochemical interaction between bubbles and blood (Ackles 1973, Ward et al 1987), endothelial damage, and microcirculatory impairment (Baz & Abdel-Khalik 1986). However, none of these findings have been sufficiently quantified for incorporation into DCS models, and consideration of their roles in the etiology of DCS is sorely lacking in even the most recent quantitative models of DCS.

DCS MODELS AND DCS PREVENTION

The primary goal of decompression theory is to prevent or control the incidence of DCS, keeping any incidence within limits of acceptable severity. Two approaches have been taken to achieve this goal: traditional deterministic and more recent probabilistic approaches. In deterministic models, a decompression is declared 'safe' if certain well-defined criteria are not violated during ascent, or 'unsafe' if any one of these ascent criteria are violated. In probabilistic approaches, DCS is recognized to be a random event that occurs with a probability that varies as a function of the conditions before, during, and after decompression. A decompression profile cannot be declared either safe or unsafe, but can only be stated to have an associated probability of DCS occurrence that the user must consider acceptable or not. An important distinction between the two approaches is that DCS outcome is explicitly modeled only in the probabilistic approach.

DETERMINISTIC DCS MODELS

The earliest models for controlling decompression, reviewed by Behnke (1975), Hills (1977), and Hempleman (1993), sought to minimize the incidence of DCS by considering its occurrence as a function of the prevailing gas supersaturation per se. Boycott et al (1908) made the seminal observation that DCS in air-breathing goats was avoided when decompressions were limited to one-half of the saturation depth. On the basis of this observation and the assumption that inspired O_2 can be neglected, it was postulated that decompressions from air dives are safe as long as they are conducted to keep tissue nitrogen tensions from exceeding 1.58 [$= 2 \cdot (1 - fo_2)$, where fo_2 is the fraction of O_2 in air] times the ambient pressure. Nitrogen tensions for control in this approach were computed using Equation 10 applied to each of a collection of parallel-perfused compartments with different inert gas exchange rates. Initially, five compartments with half-times ranging from 5 to 75 min were used. The concept of stage decompression was then introduced in order to maximize the gradient between tissue and blood periodically throughout the decompression. An important feature of this 'Haldane' method of decompression is that only a single tissue, that having the highest dissolved gas tension, controls decompression at any given time.

Decompression schedules are calculated by transforming the tissue ratio (TR; Equation 2) into a

maximum permissible tissue tension (MPTT or *M*-value) at any given stop depth. Decompression is effected by ascent to the shallowest stop before that at which a computed tissue gas tension exceeds the corresponding *M*-value. Time is then spent at that stop until all tissue gas tensions decay to values less than or equal to the *M*-values for the next stop; i.e. until the highest $p_{t,i} - M_i$ difference among the different tissues is zero; at which time the diver is decompressed to the next stop. The process is repeated at this and successive stops until the diver has surfaced, as illustrated in Fig. 10.1.17. Note that a discontinuity occurs in the maximum overpressure line when control of the decompression advances to a compartment with longer half-time. Such discontinuities are obviated in a modification of the Haldane method described by Egi & Gurmen (2000), which simplifies calculation of no-stop limits and decompression stop times as long as *M*-values can be expressed as a single continuous function of compartmental half-time and depth. Typically, low half-time tissues tend to control the deeper initial stops in a given decompression and the overall decompressions in dives of relatively short duration. High half-time tissues tend to dominate the latter shallower stops in a given decompression and the overall decompressions of longer dives.

Subsequent modifications to the Haldane method lead to specific safe ascent ratios for each tissue (Hawkins et al 1935, Yarbrough & Behnke 1939), additional tissues with longer half-times (Buhlmann 1984, Dwyer 1956, Van der Aue et al 1951), and systematic changes in the ratios with stop depth. Surfacing ratios were obtained from an ever-growing body of no-stop decompression data. Specification of how these ratios or their corresponding *M*-values should change with depth for calculation of decompression schedules became more challenging because data for such dives tended to be far less plentiful. For development of the US Navy Standard Air Decompression Tables (Des Granges 1956), Dwyer, (1956) used a complicated tenth power relationship to project surfacing *M*-values to *M*-values at the various stops. Workman, (1965) simplified this approach by expressing *M*-values for each modeled compartment in simple linear form:

$$M_i = M_{0,i} + a_i \cdot d, \qquad (39)$$

where $M_{0,i}$ and a_i are tissue-specific surfacing tension and depth-dependence parameters, respectively, and d is the depth of the next decompression stop. Table 10.1.1 gives Workman's *M* parameters for various tissue half-times. For example, the critical gas tensions in the 20 min half-time tissue for safe ascent to a depth of 10 msw are 36.8 (21.8 + 1.5 × 10) and 33.0 (20.0 + 1.3 × 10) msw for N_2 and He, respectively. Note that tissues are assumed to tolerate higher gas supersaturations with N_2 as the inert gas than with He as the inert gas.

Table 10.1.1 M_0 (in msw) and a values (see Equation 39) for nitrogen and helium.

$t_{1/2}$ (min)	N_2 Mo	a	He Mo	a
5	31.5	1.8	26.1	1.5
10	26.7	1.6	22.4	1.4
20	21.8	1.5	20.0	1.3
40	17.0	1.4	18.2	1.2
80	16.4	1.3	17.0	1.2
120	15.8	1.2	16.4	1.2
160	15.5	1.2	16.4	1.1
200	15.5	1.1	16.1	1.1
240	15.2	1.1	16.1	1.0

Assuming that the 5 min half-time compartment in Table 10.1.1 represents an aqueous tissue, then the perfusion rate can be approximated as 0.14 ml blood/ml tissue/min (Equation 8). This can be compared to values of 0.5 and 0.1 ml blood/ml tissue/min for blood flow to cerebral gray and white matter, respectively (Albano & Columba 1976). However, straightforward substitution of non-aqueous solubility values of N_2 and He for higher half-time compartments leads to conflicting values of $\dot{Q}$, thereby exposing an inconsistency in Table 10.1.1 with respect to physical and physiologic constraints. While this illustrates the highly empirical nature of the *M*-value system, Hennessey & Hempleman (1977) showed how the linear pressure-dependence of the M_i in Equation 39 follows from presumption that gas supersaturation is fully relieved by bubble formation in tissue and that DCS first occurs when the total volume of bubbles in the tissue exceeds a certain critical value. Shortly thereafter, Yount (1979a, 1981) pointed out that substitution of $(M - d)$ for P_{ss} and $(M - P_0)$ for P_{crush} in Equation 22 yields an equation of form identical to Equation 39, implying that Equation 39 specifies isopleths of constant bubble number at the threshold gas supersaturations for DCS in a given tissue.

Decompression schedules computed using M_0 values based on empirically established no-stop limits and the projection of these values to depth prescribed by Equation 39 were eventually found to be too short for longer deeper dives as they incurred unacceptably high incidences of DCS (Hempleman 1993, Workman & Bornmann 1975). This shortcoming could not be corrected without also shortening the no-stop limits, which were perceived to be acceptably short. Suitable

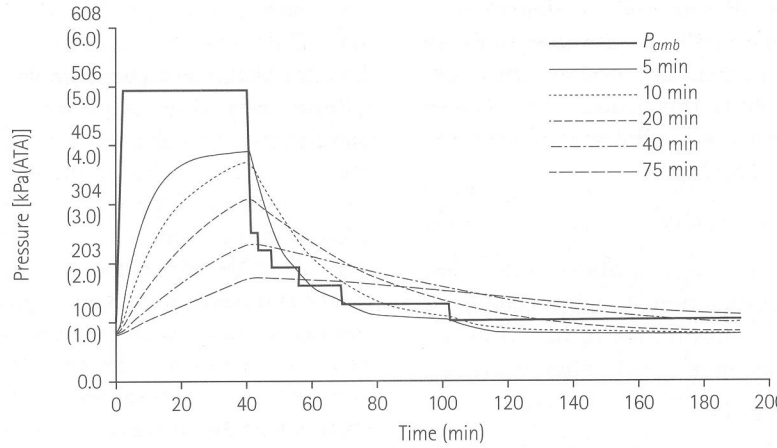

(a)

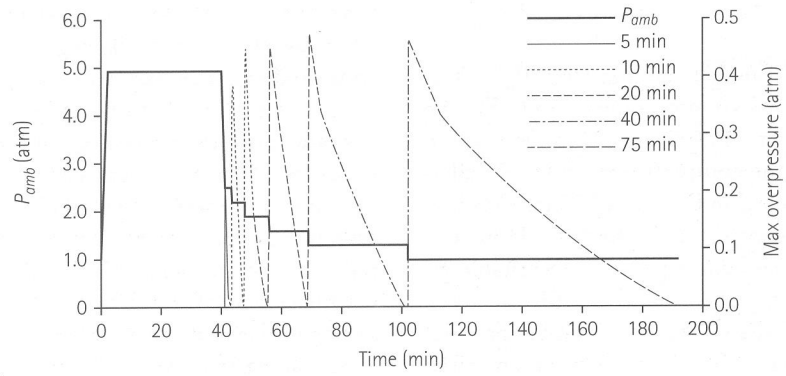

(b)

Fig. 10.1.17 Illustration of *M*-value usage in the Haldane method to compute a staged decompression for an air dive to 40 msw (130 fsw) for 40 min. (a) shows the time courses of the ambient pressure and computed dissolved N_2 tensions in each of Haldane's five compartments with indicated half-times throughout the dive. (b) shows the time courses of the ambient pressure and the maximum prevailing $p_i - M$ difference, where M is the *M*-value for the next decompression stop. Note that decompression to each stop occurs only after this difference has decayed to zero. The *M*-value at each stop depth was obtained from the Haldane tissue ratio of 1.58 for air diving; $M = 1.58 \times$ depth. As per convention, the 40 min bottom time includes descent time from surface.

lengthening of decompressions could be attained either by changing the system for specifying *M*-values or by ascribing different kinetics of tissue–blood gas exchange.

Yount & Hoffman (1986) adopted the first approach by noting that the critical volume, V_c, and critical number hypotheses are equivalent if bubbles, once nucleated, quickly attain the same size, V_b. They then postulated that a certain number of bubbles, n_0, could be tolerated without adverse effect, so that the critical volume V_c consists of the $(n - n_0)$ bubbles in excess of this tolerable number. The bubble numbers n and n_0 were assumed to be functions of compartmental gas supersaturations as prescribed by the varying permeability model of bubble nucleation described earlier. The rate at which excess undissolved gas volume, V_e, accumulates to form the critical volume in tissue is thus given by the rate of change of the excess bubble number $\times$ bubble volume product;

$$\frac{dV_e}{dt} = \frac{d[(n - n_0) \cdot V_b}{dt}, \tag{40}$$

which was simplified by fixing $(n - n_0)$ under the assumption that P_{ss} is constant throughout the decompression, unaffected by bubble formation, and equal to its value on arrival at the first decompression stop at depth d. Bubble surface tension, changes in bubble surface area with bubble size, mechanical effects, and Boyle's law effects from further decompression were also neglected so that the volume growth rate of the nucleated bubbles could be assumed

proportional to P_{ss}; i.e. $dV_b/dt = P_{ss}/\chi$. Finally, after arrival at surface at time t_d, P_{ss} was assumed to decay in the usual semiexponential fashion with the appropriate compartmental time constant, τ. Under these conditons Equation 40 is integrated over the domain of positive P_{ss} to yield:

$$V_e = (n - n_0) \cdot P_{ss} \cdot (t_d + \tau)/\chi. \quad (41)$$

Decompression is therefore considered safe with minimal total decompression time, t_d, when conducted to allow V_e to equal V_c. Substitution of $M - d$ for P_{ss} and V_c for V_e into Equation 41 yields, after rearrangement, the expression for the revised safe ascent criterion:

$$P_{ss} = \frac{\chi V_c}{(n - n_0)\cdot(t_d + \tau)}. \quad (42)$$

The corresponding M-value at the first stop, $P_{ss} + d$, is decremented at successive subsequent stops by the stop depth increment. Resultant M-values, when evaluated for each of the compartments in the parallel-perfusion model, are used in the usual Haldane fashion to compute staged decompression schedules. However, because the initial M and corresponding acceptable P_{ss} are a function of t_d, the schedule for a given decompression is calculated by an iterative process, beginning by completing the schedule using an initial estimate of P_{ss}. The t_d from this schedule is then used in Equation 42 to evaluate a new P_{ss}, complete a new schedule, and find a new t_d. The process is repeated until the acceptable P_{ss} and t_d in successive iterations differ by acceptably small amounts. With further substitution of expressions for n and n_0 from the varying permeability model, and provisions for time-dependent recovery of the nucleus radial distribution from the effects of crushing (Yount & Hoffman 1986), the new M-values become complicated functions of maximum depth and time at depth, and thus represent a substantial departure from earlier approaches based on empirically established no-stop limits. Their use generally results in deeper first stops than prescribed by earlier methods. Weinke (1990, 1992) extended this method to repetitive diving and noted that, in order to remain within the critical volume constraint, the permissible gas supersaturation $M - d$ must be reduced for decompressions in successive repetitive dives.

Gernhardt (1991) developed a different implementation of the critical released volume hypothesis (Miller et al 1973), in which he used a large R three-region model of diffusion-limited gas bubble dynamics to track bubble growth from an ever-present nucleus of fixed size in each of 10 parallel-perfused compartments in a Haldanian gas exchange model. Decompression was controlled to keep a bubble growth index, defined as the ratio of the prevailing bubble volume to the initial volume, less than a prespecified limiting value. Compartmental volumes were assumed sufficiently large compared to the bubble gas contents to warrant neglect of the $d(P_{b,g}V_b)/dt$ term in the coupled tissue tension Equation 26.

In all of the above approaches, compartmental gas uptake and elimination were assumed to be kinetically symmetric; namely, compartmental inert gas tensions were computed with the same time constants during compression and decompression phases of a dive profile. This ignored the certain effects of bubble formation via the Z_b term in Equation 6, as well as other possible effects of bubble formation on the tissue perfusion rate. These effects act together to reduce gas elimination rates after bubble formation during and after decompression compared to gas uptake rates during descent and bottom phases of each dive. In consideration of these effects, the other approach to remedy of the unacceptably short decompressions for longer and deeper dives prescribed by the earlier methods entailed introduction of kinetic asymmetry between gas uptake and elimination, with retention of surfacing M-values based on empirically established no-stop limits and the projection of these values to depth prescribed by Equation 39.

In the early development of a US Navy Real-Time Algorithm for decompression, Thalmann (1983) adopted the simplest way to implement the desired kinetic asymmetry by postulating different time constants (or half-times) for gas uptake and elimination within each compartment. However, specification of appropriate time constants for such asymmetrical (ASYM) models was completely empirical. Thalmann gave the asymmetry a biophysical basis in later work with development of the EL gas exchange model (Thalmann 1981, 1983), which explicitly considered the influence of bubble formation on gas exchange.

In the EL model, the tissue inert gas burden, $p_{t,i}$, replaces the tissue inert gas tension as the controlled quantity during decompression. The expression for the inert gas burden is obtained by rearranging Equation 26:

$$\frac{dp'_{t,g}}{dt} = \frac{dp_{t,g}}{dt} + \left(\frac{1}{a_{t,g}V_t}\right)\cdot\left(\frac{d(P_{b,g}V_b)}{dt}\right)$$
$$= \frac{[m_{a,g}t - (p_{t,g} - p^o_{a,g})]}{\tau}. \quad (43)$$

Note that $p'_{t,g}$ consists of both dissolved inert gas and inert gas in bubbles, with the latter gas treated as if it were still in solution. In the absence of bubbles, modeled

blood–tissue gas exchange follows the semiexponential function of time given by Equation 10, which is the solution of Equation 43 when $V_b = 0$. Once a bubble forms, it is assumed to be always in equilibrium with its surroundings, and effects of gas–liquid surface tension and any tissue deformation pressures are ignored. We then have the same system assumed in the derivation of Equation 27, so that in an isobaric stage, $P_{amb} - \Sigma P_{fix}$ is constant and $dp_{t,g}/dt = 0$. If the inspired p_{O_2} remains constant ($m_{a,g} = 0$), $p_{a,g}$ is also constant and equal to $p^o_{a,g}$. Hence, all components on the right of Equation 43 are constant, $dp'_{t,g}/dt$ is a negative constant, determined wholly by the $d(P_{b,g}V_b)/dt$ term, and overall gas washout from the tissue is time linear. The slowing of gas elimination under these conditions is illustrated by comparing the $p_{t,g}$ vs time curves for the highest and lowest bubble number densities in (b) of Fig. 10.1.16. Once the bubble has dissolved, the rate of gas elimination resumes the exponential behavior prescribed by Equation 10.

EL kinetics were incorporated into the Exponential-Linear MK 15/16 Real Time Algorithm with the VVAL18 MPTT Table (EL MK 15/16 RTA VVAL18) to develop the constant 70 kPa (0.7 ATA) PO_2-in-N_2 decompression tables for the USN MK 15/16 Underwater Breathing Apparatus (UBA) dived with air as the diluent gas (Thalmann 1986). A combination of ASYM and EL kinetics was used to model blood–tissue gas exchange for development of the constant 70 kPa (0.7 ATA) PO_2-in-He decompression tables for the same UBA dived with heliox as the diluent gas (Thalmann 1985).

While conceptually simple and convenient to apply, deterministic models lack a formalism for evaluating and predicting the times after decompression at which DCS is most likely to occur, and they suffer seriously from seeking only to declare a decompression either 'safe' or 'unsafe.' They cannot distinguish between different levels of safety, particularly as decompressions satisfy or violate the safe ascent criteria within different margins. This causes a somewhat subtler problem in analysis of available data – loss of information. For example, to declare an upper limit of 5% risk of DCS with 95% binomial confidence, 72 dive trials must be conducted with no incidence of DCS (Diem 1962). If, however, one incident occurs during the trials, then an additional 37 trials are required without any further incidence of DCS to defend the same 5% risk declaration. Clearly, the number of dive trials required to empirically ensure that a given profile actually incurs a low risk of DCS can quickly become untenable (see Homer & Weathersby 1985 for a more complete discussion). Weathersby et al (1984) introduced a probabilistic approach that overcomes this difficulty by allowing risk assessment based on any number of dissimilar dives. In fact, the greater the number of dives and their diversity, the more certain and generally applicable are the resultant predictions.

PROBABILISTIC DCS MODELS

In probabilistic approaches to DCS prevention, DCS is considered to be an all-or-nothing event that either occurs during a given decompression profile or does not. The probability of an observation at any time when an individual is under study is unity, consisting of the sum of the probabilities of the two mutually exclusive outcomes; that DCS has occurred $P(DCS)$ or not occurred $P(NoDCS)$:

$$P(DCS) + P(NoDCS) = 1. \tag{44}$$

The mathematical form that an expression for $P(DCS)$ must take is governed by the seemingly random nature of DCS occurrence. If, for example, a large number of individuals from a homogeneous population is exposed to a given pressure profile and the time to occurrence of DCS is determined for each individual, the number of occurrences of each DCS onset time divided by the total number of individuals in the sample might be plotted to obtain a DCS probability density distribution as shown in Fig. 10.1.18. In this figure, decompression begins at zero time on the abscissa and ends at the indicated time. The overall probability of DCS from decompression start to any time t_3 on the abscissa is given by the area under the probability density distribution between $t = 0$ and $t = t_3$ (subscripts 1 and 2 are usually reserved for conditional probabilities, hence the designation of t_3):

$$P(DCS) = \int_{t=0}^{t_3} f(t)\,dt. \tag{45}$$

DCS is most simply observed to either occur or not occur by some arbitrary time t_3 that may be common to all individuals but is always sufficiently high so that any probability of DCS after t_3 is negligible. In our example, the probability of DCS under these conditions is the same for all individuals and the observed outcome is a binary categorical response ('*DCS*' or '*NoDCS*'). With a large number of samples from the same population, this outcome is reasonably assumed to be distributed according to a binomial distribution. The observed information can then be modeled using a binary response assay in one of two forms. In the simplest of these, the DCS probability is expressed as a function of a single-valued dose variable that is computed from properties of the pressure and respired

gas profile. This approach does not require integration of a DCS probability density function, which affords it a simplicity that motivated its use as the basis of the earliest probabilistic models of DCS occurrence (Gerth et al 1992, Vann et al 1987, Weathersby et al 1984). In the other form of binary response assay, the DCS probability density function is explicitly defined and integrated over the 0–t_3 interval to obtain the DCS probability for the exposure. This approach was used as the basis for the next generation of probabilistic models of diving DCS occurrence (Weathersby et al 1985).

If the time at which DCS occurrence or non-occurrence is assessed does not meet the above criteria; i.e. is not the same for all individuals and is often low enough to miss late-occurring incidences of DCS, then both the modeled DCS probabilities and the observed outcomes become dependent on the times of the assessments. Under these conditions in our illustration, the modeled DCS probabilities and observed outcomes will no longer be the same for all individuals but will depend on time. This time dependence is taken into account by considering the outcome to be the time to DCS occurrence for those individuals that are observed to develop DCS, or the time to the end of the study for those individuals that remain DCS-free. This outcome is a continuous random variable, which, in our example, has the skewed distribution illustrated in Fig. 10.1.18, and which can be modeled using failure time, or 'survival,' analysis (Collett 1994, Kalbfleisch & Prentice 1980). Most recent probabilistic DCS models (Conkin et al 1996, Gerth & Vann 1995, 1997, Parker et al 1998, Thalmann et al 1997) use this type of analysis, which allows both the overall probability of DCS as well as the time of most probable occurrence of DCS in a profile to be estimated (Weathersby et al 1992a).

The need to specify the probability density function is a central feature both of incidence-only binary response assays and any type of survival analysis. In practice, a more readily conceptualized hazard or risk function, $h(t)$, is defined, which is itself only a transform of the probability density function:

$$h(t) = \frac{f(t)}{1 - \int_0^t f(t)\,dt}. \tag{46}$$

The hazard function gives the instantaneous probability of DCS at time t in those individuals that have not developed DCS up to time t and hence remain at risk for DCS at that time. The probability of DCS occurrence between $t = 0$ and t is then given by:

$$P(DCS_t) = 1 - P(NoDCS_t)$$
$$= 1 - exp\left(-\int_0^t h(u)\,du\right). \tag{47}$$

Any actual implementation of Equation 47 contains parameters, $\beta = (\beta_1, \beta_2, \ldots, \beta_q)$, that govern its quantitative behavior. These parameters may set location and shape properties of the hazard function for a reference population characterized by zero values for all explanatory variables, scale the influences of explanatory variables in the hazard function, or be required 'mechanistic' constants in that function. Values of these parameters required to yield model performance in best possible conformance with selected calibration data are found by maximizing a likelihood function, $L(\beta)$, of the parameters (Collett 1994, Kalbfleisch & Prentice 1980). This function is defined as the probability of the observed overall outcome of one or more exposures, given the hazard function and values for the q parameters in β. Assuming statistical independence of all possible outcomes, the likelihood, $l_i(\beta)$, of an individual exposure, i, is the product of the probabilities of the possible outcomes, each conditioned by actual experience through the influence of an outcome variable, ζ_i.

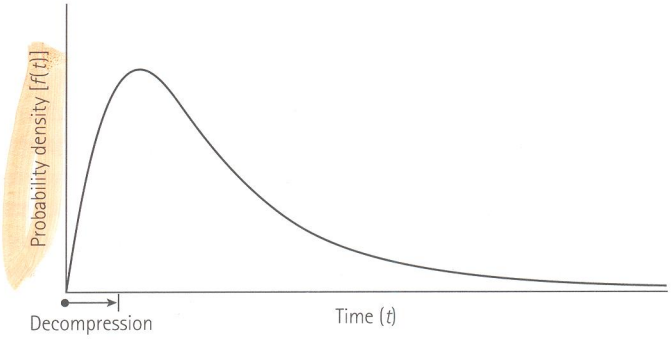

Fig. 10.1.18 Hypothetical density distribution of DCS probability after start of decompression. The initial rapid rise reflects the high frequency of DCS soon after the start of decompression relative to the number of occurrences later on.

$$l_i(\beta) = P_i(DCS)^{\xi_i} \cdot P_i(NoDCS)^{(1-\xi_i)}, \quad (48)$$

where $\zeta_i = 0$ if DCS did not occur in the exposure and $\zeta_i = 1$ if DCS did occur. $P_i(NoDCS)$ is the probability that the entire exposure is completed DCS-free. The likelihood of a trial of N independent exposures is then given as the product of the likelihoods of the individual exposures, i.e.:

$$L(\beta) = \prod_{i=1}^{N} l_i(\beta). \quad (49)$$

Parameter values are systematically adjusted to maximize Equation 49 about a data set of pressure exposures and their outcomes using iterative non-linear parameter estimation techniques (Marquardt 1963). The results are the 'best fit' values of the parameters for use in model applications and the maximum likelihood achieved by the model on the data. The latter serves as a quantitative index of model goodness-of-fit. A central and singularly most important feature of this approach is that a model is made to provide estimates of DCS risks and times of DCS occurrence that are in closest possible agreement with observed DCS incidences and times of occurrence in actual experience.

Specification of the DCS Hazard Function

Any distributional model is applicable only to populations for which the explanatory variables and factors (also called *covariates*) in the model are known and in which no other confounding factors are active to influence the modeled outcome. In other words, a model is applicable to a problem only when all relevant heterogeneity in the target population is accommodated in the covariates. In the context of DCS modeling, such heterogeneity can include exposures to multiple ambient pressures, performance of different exercises at various intensities, and breathing of different gas mixes during different periods in any given profile. Probabilistic models of DCS occurrence for practical use must therefore remain applicable to profiles of practically arbitrary complexity, which imposes certain limitations on the form for the hazard function.

Well-characterized parametric statistical distributions that incorporate the influences of covariates are readily available. For example, log-logistic models for altitude DCS have been developed that use *time-independent covariates* (Conkin et al 1996, Kannan & Raychaudhuri 1997, Kannan et al 1998). These time-independent covariates are defined with decompression profiles of a particular form in mind; i.e. with reference to one or more specific properties of the decompression profile; so that the resultant models are applicable only to decompression profiles of that form. For example, expressing DCS risk as a function of the tissue ratio in Equation 2 (Conkin et al 1996, Van Liew et al 1994) requires specification of the point in a profile at which the ratio is to be evaluated. Consideration that DCS risk may be governed by *TR* values at additional points in the profile, such as might naturally be expected in repetitive decompressions, requires addition of more covariates to the risk function, along with corresponding parameters to scale the contributions of these covariates to the risk. In general, the number of covariates and parameters in such models must increase with the complexity of the profiles to which they are applicable. In order to limit model complexity and keep the number of estimated parameters low enough to be warranted by available data, such models are limited in their ability to estimate DCS risk for complex profiles that are of usual practical interest; e.g. those that include staged or repetitive decompressions, multiple breathing gas switches, and different exercising periods.

The problem of model applicability to profiles of arbitrary complexity is solved by using *time-dependent covariates*. A model based on such covariates can respond to a covariate process (Kalbfleisch & Prentice 1980) that is external to the individual at risk and hence to the model. Because the path of the covariate process through time; e.g. the matrix of pressure, inspired gas composition, and exercise that describes the time course of exposure in a decompression problem is not fixed in the model, the model does not need to increase in complexity as the complexity of the covariate process increases. Another advantage of these models is that intermediate probabilities based on incomplete covariate vectors are readily calculated, so that the models can be used in real-time applications. 'Mechanistic' forms for the hazard function that are defined wholly in terms of explicitly-modeled physiologic process(es) have proven best able to accommodate the complexity of covariate processes encountered in practical decompression problems, while behaving in accordance with observed DCS incidences and times of DCS occurrence in large bodies of laboratory decompression data.

The challenge in hazard function design is illustrated by considering observed incidences of DCS in collections of diving and altitude exposures. The observed cumulative incidence of DCS in a large and diverse dive data set (Weathersby et al 1992b) was normalized by the total number of 921 man-dives to obtain the failure distribution, $F(t)$, as shown in Fig. 10.1.19a. The derivative of $F(t)$ yields the probability density function, $f(t)$, which defines the instantaneous risk of occurrence of DCS (Equation 46). A single-exponential

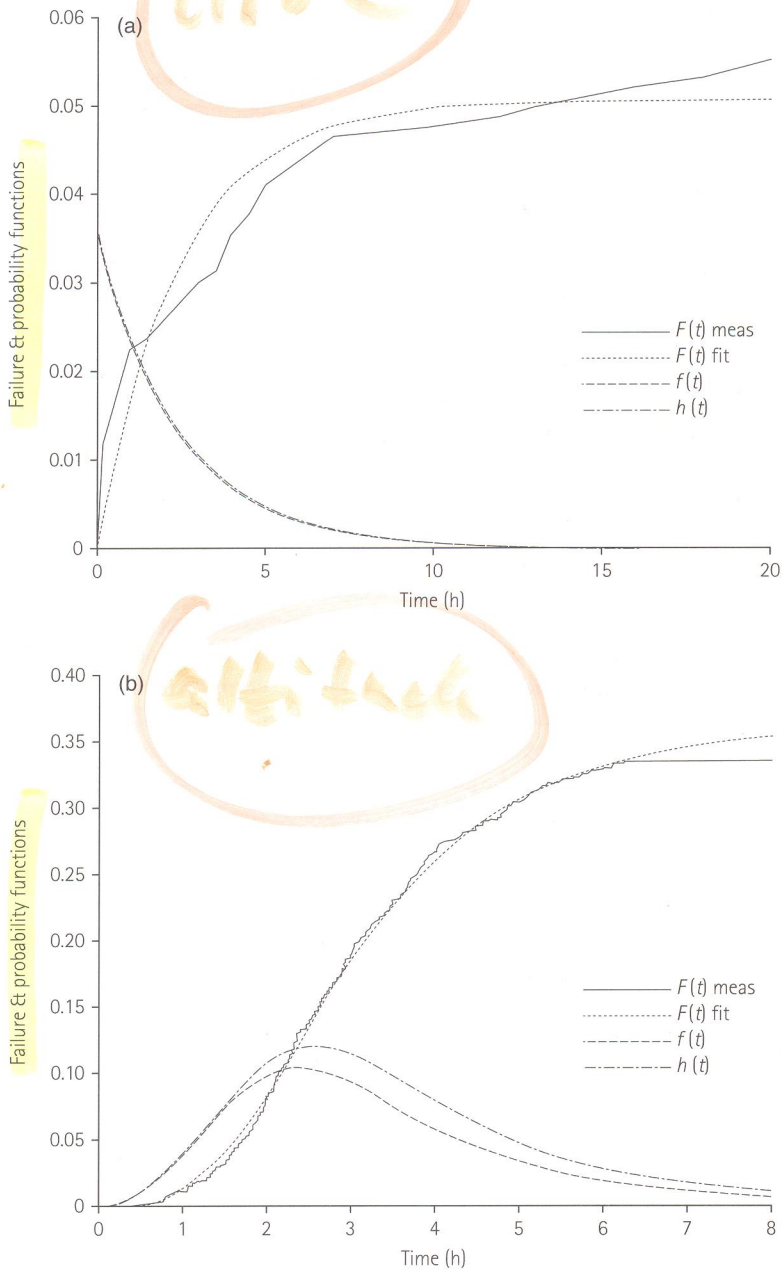

Fig. 10.1.19 The measured and fitted failure distribution of DCS incidence for (a) dives and (b) altitude excursions (see text for details). Also shown [x 100 for (a)] are the probability density function [*f(t)*] and the instantaneous risk of occurrence of DCS [*h(t)*]. Times are (a) since last reaching surface and (b) at altitude.

decay equation provides a reasonable fit of the observed distribution, as shown.

In contrast to the dive data shown in Fig. 10.1.19a, the observed distribution of DCS occurrence times after decompressions to altitude (US Air Force, courtesy of Dr A Pilmanis and the Armstrong Laboratory at Brooks AFB, TX) is distinctly sigmoidal in shape (Fig. 10.1.19b). In this case, the instantaneous risk of DCS peaks at about 2.6 h after the excursion to altitude begins, and an appropriate fit of the data is the Hill function (Vann & Thalmann 1993). These examples illustrate a fundamentally important difference in the incidence of DCS between diving and altitude exposures. Prediction models of DCS must either account for these differences or be tailored for the type of decompression involved. A major goal of DCS modeling research is to

develop a general model that accommodates both types of behavior. Fortunately, hazard functions of complexity limited only by available computational power can be specified in attempts to meet this goal.

CURRENT PROBABILISTIC MODELS OF DCS OCCURRENCE

Development of current probabilistic models of DCS has proceeded by elaboration of the original Haldanian view of the body as a collection of parallel-perfused, well-stirred compartments in which blood–tissue gas exchange is perfusion-limited. However, the reality of how DCS risk accumulates in these compartments to contribute to overall risk of DCS is fundamentally different. As pointed out earlier, only one compartment in the collection of compartments controls decompression at any one time in the Haldanian deterministic approach. In the probabilistic implementations, however, DCS is assumed able to occur independently in any of the modeled compartments at any one time. Compartmental outcomes are thus statistically independent, and the overall survivor function is the product of the individual compartmental survivor functions, $P(S_i)$, that are each given in terms of the compartmental instantaneous risk, $h_i(t)$:

$$P(S_T) = \prod_{i=1}^{m} P(S_i) = \prod_{i=1}^{m} exp\left\{-\int_0^T h_i dt\right\}$$

$$= exp\left\{-\int_0^T \sum_{i=1}^{m} h_i dt\right\}, \quad (50)$$

where m is the number of model compartments. The overall instantaneous DCS risk is therefore the sum of the compartmental hazards:

$$h(t) = \sum_{i=1}^{m} h_i(t). \quad (51)$$

As a result of this definition, all modeled compartments can contribute to DCS risk simultaneously, so that no single compartment is necessarily in control of decompression. Also, as will become clear, decompression is governed by future DCS risk, not by risk that has accumulated at one's current point in time.

USN LE1 Probabilistic Model

An appropriate form for $h(t)$ of dives represented by those depicted in Fig. 10.1.19a is the level of gas supersaturation since this value peaks upon surfacing, as demonstrated in Figs 10.1.5 and 10.1.17. For data involving only a single inert gas, this type of behavior is exhibited by the EL gas exchange model that formed the basis for the deterministic EL MK 15/16 RTA discussed earlier. Accordingly, the EL gas exchange model was chosen as the basis for the USN Linear-Exponential (LE1) probabilistic DCS model (Parker et al 1992, Thalmann et al 1997). In this model, overall instantaneous DCS risk is defined as the weighted sum of prevailing compartmental gas-supersaturation/ambient hydrostatic pressure ratios, where the gas supersaturation is defined in terms of the inert gas burden rather than the inert gas tension:

$$h(t) = \sum_{i=1}^{m} G_i\{p_{t,i} + p_{fix} - (P_{amb} + Thr_i)\}/P_{amb}, \quad (52)$$

where G and Thr are the gain and threshold parameters, respectively. The LE1 probabilistic model is 'mechanistic' in the sense that its hazard function incorporates time-dependent covariates and is completely specified in terms of a hypothetical biophysical process (although that process is never forwarded as the *real* cause of DCS). This algorithm remains one of the best available for estimating DCS probability and time of DCS occurrence in air and N_2–O_2 diving (Ball et al 1995).

Parker et al (1998) elaborated the LE1 probabilistic model to accommodate multiple inert gases in order to consider the potential influence of inspired O_2 to compartmental gas supersaturations and DCS incidence. The resultant multiple-gas LE model (LEM) incorporated kinetics following Equation 38, in which gas elimination from the tissue in the presence of one or more bubbles is no longer time-linear. A portion of the tissue O_2 tension in excess of a compartmental threshold value was then treated as inert gas by including its kinetics in the sum of the two inert gas tensions, $\sum_{g}^{2} p_{t,g}$, after removal from Σp_{fix}. Overall instantaneous DCS risk was defined as in the single-gas LE1 model, but in terms of the sum of prevailing compartmental gas burdens in excess of compartmental threshold values, Thr_i, relative to the ambient hydrostatic pressure, P_{amb}:

$$h(t) = \sum_{i=1}^{m} \frac{G_i\left\{\sum_g \frac{n_{t,g}}{a_{t,g}} + \Sigma p_{fix} - (P_{amb} + Thr_i)\right\}}{P_{amb}}. \quad (53)$$

A major limitation of the LE1 and LEM probabilistic models is that they only allow theoretical DCS risk to decrease monotonically after decompression (Gerth & Vann 1997), and are therefore intrinsically inapplicable to altitude DCS problems. A general model able to estimate DCS risk after both hypobaric and hyperbaric decompressions must accommodate both risk increases and decreases after decompression.

Bubble Volume Models

The statistical formalism of the probabilistic approach has also afforded opportunities to test various implementations of the critical released gas volume hypothesis (Miller et al 1973). All of these implementations have been mechanistic, with hazard functions defined wholly as functions of gas bubble volumes that vary in one or more parallel-perfused Haldanian gas exchange compartments in response to changes in the pressure and respired gas through an exposure profile. The first of these models incorporated the equilibrium bubble model underlying Equation 27. However, being based on the same assumptions as the deterministic EL MK 15/16 RTA and probabilistic LE1 and LEM models, modeled DCS risk could only decrease after decompression. Models in which bubble evolution is limited by gas diffusion through a barrier between bubble and tissue provided improved correlations of selected diving and altitude exposure data (Gerth et al 1992, Vann 1987, Vann et al 1987), but volume-dependent changes in bubble surface area and curvature were neglected, while changes in ambient pressure and respired gas were assumed to be instantaneous, in order to allow use of simple analytic equations for bubble dynamics (cf Equation 28).

More recent models relax the above assumptions and track bubble evolution using computation-intensive numerical solutions to bubble dynamics in one of the simple two- or three-region systems described earlier (Ball et al 1995, Gerth & Vann 1996, 1997, Tikuisis & Nishi 1994, Tikuisis et al 1994). A similar approach has also been used to model Doppler-recorded bubble incidence (Gault et al 1995).

In the bubble volume model [BVM(3)] model developed by Gerth & Vann (1996, 1997), the instantaneous DCS risk is defined as the weighted sum of the prevailing compartmental bubble volumes:

$$h(t) = \sum_{i=1}^{m} G_i\left[V_{b,i}(t) - V^o_{b,i}\right];\ V_{b,i}(t) - V^o_{b,i} \geq 0, \tag{54}$$

where for the i^{th} compartment G_i is a gain or proportionality constant, $V_{b,i}(t)$ is the bubble volume at time t and $V^o_{b,i}$ is the initial or 'nucleonic' bubble volume assumed characteristic of an ever-present pre-exisiting nucleus in the compartment. This model differs substantially in structure from the LE1 probabilistic model, but is statistically indistinguishable from the latter in its ability to correlate DCS incidences and times of occurrence in a data set of 3322 air and N_2–O_2 man-dives (Gerth & Vann 1996, 1997).

Gerth & Vann (1995) developed a single compartment bubble volume model that incorporates the varying permeability model of bubble nucleation (Yount 1979b) for application to altitude DCS data. Bubble dynamics were modeled using a three-region model with appropriate consideration of mass balance and Boyle's law effects as the bubbles nucleate during decompression. Once nucleated, all bubbles are assumed to be of the same size in order to avoid the requirement to solve the bubble dynamics equations for a population of bubbles of distributed size (Gurman 1999). The instantaneous DCS risk is given as a function of the prevailing bubble volume × bubble number density product:

$$h(t) = \frac{GN(t)\left(V_b(t) - V^o_{b,i}\right)}{V_t}. \tag{55}$$

PROBABILISTIC DECOMPRESSION

Methods for computing decompressions using a probabilistic model differ substantially from the Haldane method. The process first requires specification of an acceptable DCS risk. This can be a daunting requirement if attempted explicitly (Vann 1991, Vann & Thalmann 1993), but is more readily achieved by reference to well-established and accepted diving practices. For example, model-estimated DCS probabilities for the no-stop limits of the US Navy Standard Air Tables are given in Table 10.1.2. Results are shown from two models; BVM(3) based on Equation 55 and USN93D based on Equation 53; calibrated about the same data set of 3322 air and N_2–O_2 man-dives. The probabilities estimated by the two models for each dive are similar and vary with dive depth. Shallow dives to their no-stop limits incur higher estimated DCS risks than deep dives to their no-stop limits. The mean DCS probability for all the dives according to either model slightly exceeds 2.0%, implying that DCS risks of this magnitude are commonly, but implicitly, accepted.

Decompression from a dive that exceeds no-stop limits can be undertaken an infinite number of ways to achieve, but not exceed, a given acceptable DCS risk. However, subject to a few rules about stop depths, time increments and ascent rates, an optimum decompression schedule can be computed that minimizes total decompression time (TDT) and specifies a near-unique allocation of that time among the different stops, while incurring but not exceeding a user-specified acceptable DCS risk. Survanshi et al (1996) developed an iterative search algorithm for such computations based on the observation that decompression from a dive with a given total stop time (TST = TDT-travel time) incurs an overall $P(DCS)$ that is minimal [$= P(DCS)_{min}$] for only one or a few different allocations of the TST among the allowed stops.

Table 10.1.2 Estimated DCS probabilities [and 95% confidence limits (CL)] for the no-stop limits in the USN Standard Air Tables using the Bubble Volume Model and US Navy 93D model. (Gerth & Thalmann 1999)

Depth (msw)	(fsw)	No-stop limit (min)	P(DCS), % (95% CL) BVM(3)	USN93D
11	(35)	310	4.7 (4.0–5.4)	5.5 (4.5–6.7)
12	(40)	200	3.4 (2.9–3.9)	4.0 (3.2–5.0)
15	(50)	100	2.0 (1.6–2.6)	2.5 (2.0–3.3)
18	(60)	60	1.7 (1.2–2.3)	2.1 (1.6–2.8)
21	(70)	50	2.1 (1.5–2.7)	2.4 (1.8–3.1)
24	(80)	40	2.2 (1.6–2.9)	2.4 (1.8–3.1)
27	(90)	30	2.2 (1.6–3.0)	2.1 (1.6–2.8)
30	(100)	25	2.3 (1.6–3.1)	2.1 (1.5–2.8)
34	(110)	20	2.2 (1.6–3.1)	1.9 (1.4–2.6)
37	(120)	15	2.0 (1.3–2.9)	1.7 (1.1–2.3)
40	(130)	10	1.7 (1.0–2.7)	1.3 (0.8–2.1)
43	(140)	10	1.9 (1.2–3.0)	1.5 (0.9–2.2)
46	(150)	5	1.4 (0.7–2.6)	1.1 (0.6–1.9)
49	(160)	5	1.5 (0.8–2.8)	1.2 (0.6–2.0)
52	(170)	5	1.7 (0.8–3.1)	1.2 (0.7–2.1)
55	(180)	5	1.8 (0.9–3.3)	1.3 (0.7–2.2)
58	(190)	5	2.0 (1.0–3.5)	1.3 (0.8–2.2)
		Mean =	2.2	2.1

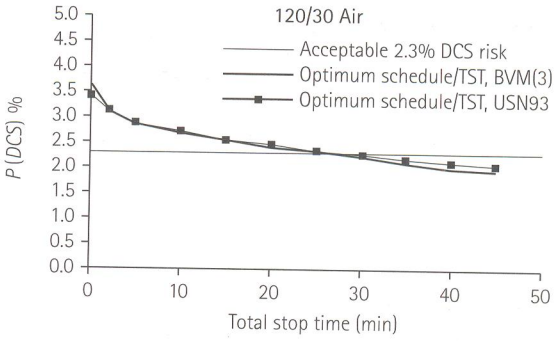

120/30 Air	BVM(3) [nbs443c]	USN93 [nbn1x3g]
TST	27	30
Stops	60/1	50/1
	50/9	40/2
	40/15	30/21
	20/1	20/3
	10/1	10/3

Fig. 10.1.20 Minimum DCS probability vs total stop time for decompressions from a 30 min, 37 msw (120 fsw) air dive. Under the BVM(3) model, the schedule with $P(DCS)_{min}$ that intersects the acceptable DCS risk line has a TST of 27 min as indicated by the arrow. This is the shortest or 'optimum' schedule for which the estimated DCS probability equals the acceptable DCS risk.

For example, Fig. 10.1.20 shows the dependence of $P(DCS)_{min}$ on TST for decompression from a 30 min, 37 msw (120 fsw) air dive as estimated using the BVM(3) model. The figure includes a horizontal line showing a constant 2.3% acceptable DCS risk. The intersection of the $P(DCS)_{min}$/TST line with the acceptable DCS risk line occurs at the shortest TST that incurs a DCS probability equal to the acceptable risk. The corresponding schedule is the 'optimum' decompression schedule for the dive. For the dive illustrated, this optimum schedule has a TST of 27 min, with 10 min at 15 msw (50 fsw), 15 min at 12 msw (40 fsw), 1 min at 6 msw (20 fsw) and 1 min at 3 msw (10 fsw). Note that the dive can be a no-stop dive under either model if the acceptable risk is allowed to exceed about 3.6%. Also large increases in TST are required to effect relatively small decreases in DCS risk due to the low slope of the $P(DCS)_{min}$/TST line.

DCS risk accumulates during and after decompression to attain the overall probability of DCS for the exposure. Unlike the instantaneous DCS risk, however, the cumulative probability can only remain unchanged or increase over time. As a result, continued or repetitive exposures ultimately force consideration only of risk to be faced in the future, with neglect of risk that has been survived in the past. The corresponding cumulative DCS risk is the conditional probability of DCS; i.e. the probability that DCS will occur in the future, given that DCS has not occurred up to the present time. Conditional probability is particularly useful for adapting probabilistic models to real-time applications (Survanshi et al 1996) and for planning repetitive dives (Survanshi et al 1997).

MODEL SHORTCOMINGS AND FUTURE DIRECTIONS

Present decompression theory, for practical purposes at least, does not appear seriously deficient in its treatments of gas exchange and bubble growth. However, DCS models that incorporate even the most advanced of these treatments remain incomplete. When used to prescribe decompression procedures, they all purposely allow some degree of bubble formation in order to reach an acceptable balance between productive bottom time, decompression obligation, risks of DCS, and other hazards. But they invariably focus on the control of gas supersaturation and bubble formation per se, and fail to explicitly consider what happens when the 'allowed' bubbles set in motion any train of events that leads to problems even after the bubbles have diminished or resolved.

Indeed, there is widespread evidence that the occurrence of at least some forms of DCS is not entirely consistent with purely physical processes. As an arguable result, inability to predict or control DCS severity is perhaps the most glaring deficiency of modern DCS prevention algorithms. This is largely due to the relatively mild nature of the DCS cases that are in the data available for model calibration. Because purposeful experimentation to severe outcomes is impossible with humans, expansion of model capability to cover more severe cases will require an improved understanding of how changes in bubble location, size, and profusion translate into changes in DCS severity, and an ability to quantitatively scale results from animal experiments to humans.

These and other outstanding issues will be met by settling present uncertainties about the bubble nucleation mechanisms that govern the distribution and profusion of bubbles in vivo, and by developing more complete and quantitative understanding of the biochemical and physiologic links between bubbles and DCS, and of the influences of anthropometric factors, exercise (Kumar & Powell 1994, Van der Aue et al 1949, Vann 1982, Vann et al 1989), and thermal stress (Leffler 2001). Additionally, risks of O_2 toxicity presently limit more aggressive exploitation of the O_2 window. An improved understanding of O_2 toxicity leading to even small increases in acceptable P_{O_2} exposures under different conditions is anxiously awaited for translation into more efficient decompression procedures.

Ultimately, the greatest challenge will be met when all relevant factors are synthesized into a quantitative model that is generally applicable to all types of hypo- and hyperbaric decompressions.

GLOSSARY OF SYMBOLS

VARIABLES:

a	model parameter
c	gas concentration
d	depth
D	diffusion coefficient
$f(t)$	probability density function
$F(t)$	failure distribution
G	model parameter
h	bubble boundary layer thickness
$h(t)$	hazard or risk function
J	gas flux
k	Boltzmann gas constant
K	rate of gas absorption
l,L	*likelihood function*
$m_{a,g}$	rate of change of arterial gas tension
M	Workman's M-value
N	*bubble population*
n_g	moles of gas
p	gas tension
P	pressure (subscripted); probability (unsubscripted)
$p_{a(v)}$	arterial (venous) gas tension
P_{amb}	ambient gas pressure
P_{ss}	gas supersaturation
$\dot{Q}$	blood perfusion rate
R	bubble radius
R_c	critical radius
S	survivor function
t	time
T	temperature
Thr	model parameter
TR	tissue ratio
V	volume
W_{rev}	free energy of formation of critical-size bubble
Z	gas consumption rate; Zeldovich factor
α	gas solubility
β	Yount shape factor; model parameter
κ	gas transfer coefficient
δ	deformation pressure; outcome variable
τ	time constant
Γ	interfacial spreading coefficient
χ	proportionality factor
γ	surface tension
γ_c	Yount crumbling pressure

SUBSCRIPTS:

b	bubble
g	gas
i	inert gas component
fix	metabolic gases and water vapor
o	initial state (also superscripted)
t	tissue

References

Ackles KN. Blood-bubble interaction in decompression sickness. DCIEM Conference Proceedings No. 73-CP-960, Toronto, CA: Defence and Civil Institute of Environmental Medicine; 1973.

Albano G, Columba M. Inert gas absorption and elimination kinetics in spinal cord. In: Lambertsen CJ, ed. Underwater physiology V. Bethesda, MD: Federation of American Societies for Experimental Biology; 1976: 355–363.

Apfel RE. Vapor nucleation at a liquid–liquid interface. J Chem Phys 1971; 54:62–63.

Ball R, Himm J, Homer LD, et al. Does the time course of bubble evolution explain decompression sickness risk? Undersea Hyperb Med 1995; 22:263–280.

Baz A, Abdel-Khalik SI. Effect of intravascular bubbles on perfustae flow and gas elimination rates following simulated decompression of a model tissue. Undersea Biomed Res 1986; 13(1):27–44.

Behnke AR. Early quantitative studies of gas dynamics in decompression. In: Bennett P, Elliott D, eds. The physiology and medicine of diving. 2nd edn. London: Baillière Tindall; 1975: 392–416.

Behnke AR, Yarbrough OD. Respiratory resistance, oil-water solubility, and mental effects of argon compared with helium and nitrogen. Am J Physiol 1939; 126:409–415.

Blander M. Bubble nucleation in liquids. Adv Colloid Interface Sci 1979; 10:1–32.

Boycott AE, Damant GCC, Haldane JB. The prevention of compressed air illness. J Hyg Lond 1908; 8:342–443.

Brubakk AO, Vik A, Flook V. Gas bubbles and the lungs. In: Lundgren CEG, Miller JN, eds. The lung at depth. New York, NY: Marcel Dekker; 1999: 237–294.

Buhlmann AA. Decompression – decompression sickness Berlin: Springer-Verlag; 1984.

Christoforides C, Hedley-Whyte J. Solubility of N_2O, N_2, and He in human whole blood and water: Constant relative solubility of N_2O. Fed Proc 1970; 29:A330.

Collett D. Modelling survival data in medical research. London: Chapman & Hall; 1994.

Conkin J, Kumar K, Powell MR, et al. A probabilistic model of hypobaric decompression sickness based on 66 chamber tests. Aviat Space Environ Med 1996; 67.

Crum LA, Hansen GM. Growth of air bubbles in tissue by rectified diffusion. Physics Med Biol 1982; 27(3):413–418.

Crum LA, Mao Y. Acoustically enhanced bubble growth at low frequencies and its implications for human diver and marine mammal safety. J Acoust Soc Am 1996; 99(5):2898–2907.

Crum LA, Daniels S, ter Haar GR, et al. Ultrasonically induced gas bubble production in agar based gels: Part II, theoretical analysis. Ultrasound Med Biol 1987; 13(9):541–554.

Dalecki D, Raeman CH, Child SZ, et al. Remnants of Albunex® nucleate acoustic cavitation. Ultrasound Med Biol 1997; 23(9):1405–1412.

Daniels S, Eastaugh KC, Paton WDM, et al. Micronuclei and bubble formation: a quantitative study using the common shrimp, *Crangon crangon*. In: Bachrach AJ, Matzen MM, eds. Underwater physiology VIII: Proceedings of the 8th Symposium on Underwater Physiology. Bethesda, MD: Undersea and Hyperbaric Medical Society; 1984: 147–157.

DCIEM Diving Manual, Part 2. Helium–oxygen surface-supplied decompression procedures and tables. Richmond, BC, Canada: Universal Dive Techtronics; 1995.

Des Granges M. Standard Air Decompression Tables. Research Report 5–57. Washington, DC: US Navy Experimental Diving Unit; 1956.

Diem K. Documenta geigy scientific tables, 6th edn. New York: Ardsley, Geigy Chem Corp; 1962.

Dwyer JV. Calculation of air decompression tables. Research Report 4–56. Washington, DC: US Navy Experimental Diving Unit; 1956.

Egi SM, Gurmen NM. Computation of decompression tables using continuous compartment half-lives. Undersea Hyperb Med 2000; 27:143–153.

Evans A, Walder DN. Significance of gas micronuclei in the aetiology of decompression sickness. Nature 1969; 222:251–252.

Farhi LE, Olszowka J. Analysis of alveolar gas exchange in the presence of soluble inert gases. Respir Physiol 1968; 5:53–67.

Finkelstein Y, Tamir A. Formation of gas bubbles in supersaturated solutions of gases in water. Am Inst Chem Eng J 1985; 31:1409–1419.

Flook V. Application of an advanced physiological model of decompression in the evaluation of decompression stress. Offshore Technology Report – OTO 98 090, UK: Health & Safety Executive; 1998.

Foster PP, Conkin J, Powell MR, et al. Role of metabolic gases in bubble formation during hypobaric exposures. J Appl Physiol 1998; 84:1088–1095.

Fox FE, Herzfeld KF. Gas bubbles with organic skin as cavitation nuclei. J Acoust Soc Am 1954; 26:984–989.

Fyrillas MM, Szeri AJ. Dissolution or growth of soluble spherical oscillating bubbles. J Fluid Mechanics 1994; 277:381–407.

Gault KA, Tikuisis P, Nishi RY. Calibration of a bubble evolution model to observed bubble incidence in divers. Undersea Hyperb Med 1995; 22:249–262.

Gernhardt ML. Development and evaluation of a decompression stress index based on tissue bubble dynamics. University of Pennsylvania. Ann Arbor, MI: University Microfilms International; 1991.

Gerth WA. Studies of spontaneous bubble nucleation in gas-supersaturated liquids in vitro with implications for in vivo bubble formation. University of San Diego, CA: University of California; 1979.

Gerth WA, Hemmingsen EA. Gas supersaturation thresholds for spontaneous cavitation in water with gas equilibration pressures up to 570 ATM. Zeitschr Naturforsch 1976; 31a:1711–1716.

Gerth WA, Hemmingsen EA. Heterogeneous nucleation of bubbles at solid surfaces in gas-supersaturated aqueous solutions. J Colloid Interface Sci 1980; 74:80–89.

Gerth WA, Thalmann ED. Estimated DCS risks of reverse dive profiles. In: Lang MA, Lehner CE, eds. Proceedings of Reverse Dive Profiles Workshop. Washington, DC: Smithsonian Institution; 1999; 145–170.

Gerth WA, Vann RD. Statistical bubble dynamics algorithms for assessment of altitude decompression sickness incidence. AL/CF-TR-1995-0037. Brooks Air Force Base, TX; 1995.

Gerth WA, Vann RD. Development of Iso-DCS risk air and nitrox decompression tables using statistical bubble dynamics models. Final Report, Contract # NA46RU0505.

Bethesda, MD: National Oceanic and Atmospheric Administration, Office of Undersea Research; 1996.
Gerth WA, Vann RD. Probabilistic gas and bubble dynamics models of DCS occurrence in air and N_2O_2 diving. Undersea Hyperb Med 1997; 24:275–292.
Gerth WA, Vann RD, Southerland DG. Quasi-physiological decompression sickness incidence modeling. In: Lang MA, Vann RD, eds. Proceedings of Repetitive Diving Workshop. Costa Mesa, CA: American Academy of Underwater Sciences; 1992.
Gurman NM. The dynamics of bubble spectra in tissues. University of South Florida. University Microfilms International, Ann Arbor, MI; 1999.
Harvey EN. Physical factors in bubble formation. In: Fulton JF, ed. Decompression sickness. Philadelphia: WB Saunders 1951: 90–114.
Harvey NE, Barnes DK, McElroy WD, et al. Bubble formation in animals. I. Physical factors. J Cell Compar Physiol 1944; 24:1–22.
Hawkins JA, Shilling CW, Hansen RA. A suggested change in calculating decompression tables. US Naval Medical Bulletin 1935; 33:327–338.
Hayward ATJ. Tribonucleation of bubbles. Br J Appl Phys 1967; 18:641–644.
Hemmingsen EA. Cavitation in gas-supersaturated solutions. J Appl Phys 1975; 46:213–218.
Hemmingsen EA. Effects of surfactants and electrolytes on the nucleation of bubbles in gas-supersaturated solutions. Zeitschrift fur Naturforschung 1978; 33a:164–171.
Hemmingsen EA. Nucleation of bubbles in vitro and in vivo. In: Brubakk AO, Hemmingsen BB, Sundnes G, eds. Supersaturation and bubble formation in fluids and organisms. Trondheim, Norway: Tapir; 1989.
Hempleman HV. British decompression theory. In: Bennett PB, Elliott DH, eds. The physiology and medicine of diving and compressed air work. Baltimore, MD: Williams and Wilkins; 1969: 291–318.
Hempleman HV. History of decompression procedures. In: Bennett P, Elliott D, eds. The physiology and medicine of diving. 4th edn. London: WB Saunders; 1993: 324–375.
Hennessey TR. The equivalent bulk diffusion model of the pneumatic decompression computer. Med Biol Eng 1973; 11:135–137.
Hennessy TR. On the site, origin, evolution and effects of decompression microbubbles. In: Brubakk AO, Hemmingsen BB, Sundnes G, eds. Supersaturation and bubble formation in fluids and organisms. Trondheim, Norway: Tapir; 1989.
Hennessy TR, Hempleman HV. An examination of the critical released gas volume concept in decompression sickness. Proceedings of the Royal Society of London 1977; 197:299–313.
Hills BA. Decompression sickness: A study of cavitation at the liquid–liquid interface. Aerospace Med 1967; 38:814–817.
Hills BA. Decompression sickness: the biophysical basis of prevention and treatment. Chichester, UK: John Wiley; 1977.
Hlastala MP, Van Liew HD. Absorption of in vivo inert gas bubbles. Respir Physiol 1975; 24:147–158.
Homer LD, Weathersby PK. Statistical aspects of the design and testing of decompression tables. Undersea Hyperb Med 1985; 12:239–249.
Homer LD, Weathersby PK. How well mixed is inert gas in tissues? J Appl Physiol 1986; 60:2079–2088.
Homer LD, Weathersby PK, Survanshi S. How countercurrent blood flow and uneven perfusion affect the motion of inert gas. J Appl Physiol 1990; 69:162–170.
Ikels KG. Production of gas bubbles in fluids by tribonucleation. J Appl Physiol 1970; 28:524–527.
Jiang Y, Homer LD, Thalmann ED. Development and interactions of two inert gas bubbles during decompression. Undersea Hyperb Med 1996; 23:131–140.
Kalbfleisch JD, Prentice RL. The statistical analysis of failure time data. New York: Wiley; 1980.
Kannan N, Raychaudhuri A. Survival models for predicting altitude decompression sickness. AL/CF-TR-1997-0030, Brooks Air Force Base, TX; 1997.
Kannan N, Raychaudhuri A, Pilmanis AA. A loglogistic model for altitude decompression sickness. Aviation Space Environ Med 1998; 69:965–970.
Kidd DJ, Stubbs RA. The use of the pneumatic analog computer for divers. In: Bennett PB, Elliott D, eds. The physiology and medicine of diving and compressed air work. 1st edn. London: Baillière, Tindall and Cassell; 1969: 386–413.
Kislyakov YY, Kopyltsov AV. The rate of gas-bubble growth in tissue under decompression. Mathematical modelling. Respir Physiol 1988; 71:299–306.
Kumar KV, Powell MR. Survivorship models for estimating the risk of decompression sickness. Aviation Space Environ Med 1994; 65:661–665.
Leffler CT. Effect of ambient temperature on the risk of decompression sickness in surface decompression divers. Aviat Space Environ Med 2001; 72:477–483.
Lewis GN, Randall M. Thermodynamics. 2nd edn. New York: McGraw-Hill; 1961.
Lobdell DD. An invertible simple equation for computation of blood O_2 dissociation relations. J Appl Physiol 1981; 50(5):971–973.
McDonough PM, Hemmingsen EA. Bubble formation in crabs induced by limb motions after decompression. J Appl Physiol 1984a; 57:117–122.
McDonough PM, Hemmingsen EA. Bubble formation in crustaceans following decompression from hyperbaric gas exposures. J Appl Physiol Respir Environ Exercise Physiol 1984b; 56:513–519.
Mapleson WW. An electrical analogue for uptake and exchange of inert gases and other agents. J Appl Physiol 1963; 18:197–204.
Marquardt DW. An algorithm for least-squares estimation of nonlinear parameters. J Soc Ind Appl Math 1963; 11:431–441.
Meisel S, Nir A, Kerem D. Bubble dynamics in perfused

tissue undergoing decompression. Respir Physiol 1981; 43:89–98.

Miller KW, Paton WDM, Smith RA. The pressure reversal of general anesthesia and the critical volume hypothesis. Mol Pharmacol 1973; 9:131–143.

Nims LF. Environmental factors affecting decompression sickness. In: Fulton JF, ed. Decompression sickness. Philadelphia, PA: WB Saunders; 1951: 192–222.

Nishi RY. Doppler and ultrasonic bubble detection. In: Bennett PB, Elliott DH, eds. The physiology and medicine of diving. 4th edn. London: WB Saunders; 1993: 433–453.

Olszowka AJ, Farhi LE. A digital computer program for constructing ventilation-perfusion lines. J Appl Physiol 1969; 26:141–146.

Otis DR Jr, Ingenito EP, Kamm RD, et al. Dynamic surface tension of surfactant TA: Experiments and theory. J Appl Physiol 1994; 77:2681–2688.

Parker EC, Survanshi SS, Weathersby PK, et al. Statistically based decompression tables VIII: Linear-exponential kinetics. NMRI Technical Report 92–73. Bethesda, MD: Naval Medical Research Institute; 1992.

Parker EC, Survanshi SS, Massell PB, et al. Probabilistic models of the role of oxygen in human decompression sickness. J Appl Physiol 1998; 84:1096–1102.

Sette D. Research on cavitation nuclei. In: Albers VM, ed. Underwater acoustics. New York, NY: Plenum Press, 1967; 139–160.

Sette D, Wanderlingh F. Thermodynamic theory of bubble nucleation induced in liquids by high energy particles. J Acoust Soc Am 1967; 41:1072–1082.

Srinivasan RS, Gerth WA, Powell MR. Mathematical models of diffusion-limited gas bubble dynamics in tissue. J Appl Physiol 1999; 86:732–741.

Srinivasan RS, Gerth WA, Powell MR. A mathematical model of diffusion-limited gas bubble dynamics in tissue with varying diffusion region thickness. Respir Physiol 2000; 123:153–164.

Survanshi SS, Weathersby PK, Thalmann ED. Statistically based decompression tables X: Real-time decompression algorithm using a probabilistic model. NMRI 96–06. Bethesda, MD: Naval Medical Research Institute; 1996.

Survanshi SS, Parker EC, Thalmann ED, et al. Statistically based decompression tables XII: Volume I. Repetitive decompression tables for air and constant 0.7 ATA PO_2 in N_2 using a probabilistic model. NMRI 97–36. Vol I. Bethesda, MD: Naval Medical Research Institute; 1997.

Thalmann ED. Refinement of 0.7 ATA oxygen in nitrogen decompression tables. Undersea Biomed Res 1981; 8(suppl):8(Abstract).

Thalmann ED. Computer algorithms used in computing the MK 15/16 constant 0.7 ATA oxygen partial pressure decompression tables. NEDU Report No. 1–83. Panama City, FL: Navy Experimental Diving Unit; 1983.

Thalmann ED. Development of a decompression algorithm for constant 0.7 ATA oxygen partial pressure in helium diving. NEDU Report 1–85. Panama City, FL: Navy Experimental Diving Unit; 1985.

Thalmann ED. Air-N_2O_2 decompression computer algorithm development. NEDU Report 8–85. Panama City, FL: Navy Experimental Diving Unit; 1986.

Thalmann ED, Parker EC, Survanshi SS, et al. Improved probabilistic decompression model predictions using linear-exponential kinetics. Undersea Hyperb Med 1997; 24(4):255–274.

Tikuisis P. Modeling the observations of in vivo bubble formation with hydrophobic crevices. Undersea Biomed Res 1986; 13:165–180.

Tikuisis P, Nishi RY. Role of oxygen in a bubble model for predicting decompression illness. DCIEM Report No. 94–04. Toronto, Canada: Defence and Civil Institute of Environmental Medicine; 1994.

Tikuisis P, Ward CA, Venter RD. Bubble evolution in a stirred volume of liquid closed to mass transport. J Appl Phys 1983; 54:1–9.

Tikuisis P, Gault KA, Nishi RY. Prediction of decompression illness using bubble models. Undersea Biomed Res 1994; 21:129–143.

Tucker AS, Ward CA. Critical state of bubbles in liquid–gas solutions. J Appl Phys 1975a; 46:4801–4808.

Tucker AS, Ward CA. Thermodynamic theory of diffusion-controlled bubble growth or dissolution and experimental examination of the predictions. J Appl Phys 1975b; 46:233–238.

Van der Aue OE, Kellar RJ, Brinton ES. The effect of exercise during decompression from increased barometric pressures on the incidence of decompression sickness. Research Report 8–49. Washington, DC: US Navy Experimental Diving Unit; 1949.

Van der Aue OE, Keller RJ, Brinton ES, et al. Calculation and testing of decompression tables for air dives. Research Report MM 002.007. Washington, DC: US Navy Experimental Diving Unit; 1951.

Van Liew HD, Burkard ME. Density of decompression bubbles and competition for gas among bubbles, tissue and blood. J Appl Physiol 1993; 75:2293–2301.

Van Liew HD, Burkard ME. Bubbles in circulating blood: stabilization and simulations of cyclic changes of size and content. J Appl Physiol 1995; 79:1379.

Van Liew HD, Hlastala MP. Influence of bubble size and blood perfusion on absorption of gas bubbles in tissues. Respir Physiol 1969; 7:111–121.

Van Liew HD, Raychaudhuri S. Stabilized bubbles in the body: pressure–radius relationships and the limits to stabilization. J Appl Physiol 1997; 82:2045–2053.

Van Liew HD, Conkin J, Burkard ME. The oxygen window and decompression bubbles: Estimates and significance. Aviat Space Environ Med 1993; 64:859–865.

Van Liew HD, Conkin J, Burkhard ME. Probabilistic model of altitude decompression sickness based on mechanistic principle. J Appl Physiol 1994; 76(6):2726–2734.

Vann RD. Decompression theory and applications. In: Bennett PB, Elliott DH, eds. The physiology and medicine of diving and compressed air work. 3rd edn. London: Baillière Tindall; 1982:352–382.

Vann RD. Likelihood analysis of decompression data using

Haldane and bubble growth models. In: Bove AA, Bachrach AJ, Greenbaum LJ, eds. Proceedings of the 9th International Symposium on Underwater and Hyperbaric Physiology. Bethesda, MD: Undersea and Hyperbaric Medical Society; 1987: 165–181.

Vann RD. Vacuum phenomena: An annotated bibliography. In: Vann RD, ed. The physiological basis of decompression: Proceedings of the 38th UHMS Workshop. Bethesda, MD: Undersea and Hyperbaric Medical Society; 1989: 179–195.

Vann RD. The use of risk analysis to develop decompression procedures. In: Sterk W, Hamilton RW, eds. Operational dive and decompression data: collection and analysis. (DATA) 17-8-90. Amsterdam, The Netherlands: European Undersea Biomedical Society; 1991:100–106.

Vann RD, Thalmann ED. Decompression physiology and practice. In: Bennett PB, Elliott DH, eds. The physiology and medicine of diving. 4th edn. London: WB Saunders; 1993: 376–432.

Vann RD, Gerth WA, Leatherman NE, et al. A likelihood analysis of experiments to test altitude decompression protocols for Shuttle operations. Aviat Space Environ Med 1987; 58(9, suppl):A106–A109.

Vann RD, Gerth WA, Leatherman NE. Exercise and decompression sickness. In: Vann RD, ed. The physiological basis of decompression. Bethesda, MD: Undersea and Hyperbaric Medical Society; 1989.

Walder DN, Evans A. In vivo nuclear fission in the aetiology of decompression sickness. Nature 1974; 252:696–697.

Ward CA. The rate of gas absorption at a liquid interface. J Chem Phys 1977; 67:229–235.

Ward CA, Balakrishnan A, Hooper FC. On the thermodynamics of nucleation in weak gas liquid solutions. J Basic Eng 1970; 92:695–704.

Ward CA, Rizk M, Tucker AS. Statistical rate theory of interfacial transport. II. Rate of isothermal bubble evolution in a liquid–gas solution. J Chem Phys 1982a; 76:5605–5614.

Ward CA, Tikuisis P, Venter RD. Stability of bubbles in a closed volume of liquid–gas solution. J Appl Phys 1982b; 53:6076–6084.

Ward CA, Tikuisis P, Tucker AS. Bubble evolution in solutions with gas concentrations near the saturation value. J Colloid Interface Sci 1986; 113:388–398.

Ward CA, McCullough D, Fraser WD. Relation between complement activation and susceptibility to decompression sickness. J Appl Physiol 1987; 62:1160–1166.

Weathersby PK, Homer LD. Solubility of inert gases in biological fluids and tissues: A review. Undersea Biomed Res 1980; 7:277–296.

Weathersby PK, Mendenhall KG, Barnard EEP, et al. Distribution of xenon gas exchange rates in dogs. J Appl Physiol 1981; 50:1325–1336.

Weathersby PK, Homer LD, Flynn ET. Homogeneous nucleation of gas bubbles in vivo. J Appl Physiol 1982; 53:940–946.

Weathersby PK, Homer LD, Flynn ET. On the likelihood of decompression sickness. J Appl Physiol Resp Environ Exercise Physiol 1984; 57(3):815–825.

Weathersby PK, Survanshi SS, Homer LD, et al. Statistically based decompression tables I: Analysis of standard air dives: 1950–1970. NMRI 85-16. Bethesda, MD: Naval Medical Research Institute; 1985.

Weathersby PK, Survanshi SS, Homer LD, et al. Predicting the time of occurrence of decompression sickness. J Appl Physiol 1992a; 72(4):1541–1548.

Weathersby PK, Survanshi SS, Nishi RY, et al. Statistically based decompression tables VII: Selection and treatment of primary air and N_2O_2 data. NSMRL Report 11-82/NMRI Report 92-85. Bethesda, MD: Joint Report: Naval Submarine Medical Research Laboratory and Naval Medical Research Institute; 1992b.

Wienke BR. Tissue gas exchange models and decompression computations: A review. Undersea Biomed Res 1989; 16:53–89.

Wienke BR. Reduced gradient bubble model. Int J Biomed Comput 1990; 26:237–256.

Wienke BR. Numerical phase algorithm for decompression computers and applications. Comput Biol Med 1992; 22:389–406.

Workman RD. Calculation of decompression schedules for nitrogen–oxygen and helium–oxygen dives. Research Report 6–65. Washington, DC: US Navy Experimental Diving Unit; 1965.

Workman RD, Bornmann RC. Decompression theory: American practice. In: Bennett PB, Elliott D, eds. The physiology and medicine of diving. 2nd edn. London: Baillière Tindall; 1975: 307–330.

Yarbrough OD, Behnke AR. The treatment of compressed-air illness utilizing oxygen. J Indust Hyg Toxicol 1939; 21:213–218.

Yount DE. Skins of varying permeability: A stabilization mechanism for gas cavitation nuclei. J Acoust Soc Am 1979a; 65:1429–1439.

Yount DE. Application of a bubble formation model to decompression sickness in rats and humans. Aviat Space Environ Med 1979b; 50:44–50.

Yount DE. Application of a bubble formation model to decompression sickness in fingerling salmon. Undersea Biomed Res 1981; 8:199–208.

Yount DE. On the evolution, generation, and regeneration of gas cavitation nuclei. J Acoust Soc Am 1982; 71:1473–1481.

Yount DE. A model for microbubble fission in surfactant solutions. J Colloid Interface Sci 1983; 91:349–360.

Yount DE. On the elastic properties of the interfaces that stabilize gas cavitation nuclei. J Colloid Interface Sci 1997; 193:50–59.

Yount DE, Hoffman DC. On the use of a bubble formation model to calculate diving tables. Aviat Space Environ Med 1986; 57:149–156.

Yount DE, Kunkle TD. Gas nucleation in the vicinity of solid hydrophobic spheres. J Appl Phy 1975; 46:4484–4486.

Yount DE, Lally DA. On the use of oxygen to facilitate decompression. Aviat Space Environ Med 1980; 51:544–550.